

BMO TR-81-2

SAI DOCUMENT NO. SAI-067-81R-010

2
LEVEL III
A108846

**PERFORMANCE TECHNOLOGY PROGRAM
(PTP-S II)**

VOLUME V

**INFRARED MAPPING OF BOUNDARY LAYER TRANSITION
ON A SLENDER CONE**

SCIENCE APPLICATIONS, INC.
APPLIED MECHANICS OPERATION
WAYNE, PENNSYLVANIA 19087

APRIL, 1980

FINAL REPORT FOR PERIOD MARCH 1978 - DECEMBER 1979

CONTRACT NO. F04701-77-C-0126

APPROVED FOR PUBLIC RELEASE; DISTRIBUTION UNLIMITED.

AIR FORCE BALLISTIC MISSILE OFFICE
NORTON AIR FORCE BASE, CALIFORNIA 92409

DTIC
ELECTE
S
DEC 28 1981

D

412706
81 12 23 120

DTIC FILE COPY

AD A108847

This final report was submitted by Science Applications, Inc., 1200 Prospect Street, La Jolla, California 92038, under Contract Number FO4701-77-C-0126 with the Ballistic Missile Office, AFSC, Norton AFB, California. Major Kevin E. Yelmgren, BMO/SYDT, was the Project Officer in charge. This technical report has been reviewed and is approved for publication.

Kevin E. Yelmgren

KEVIN E. YELMGREN, Major, USAF
Chief, Vehicle Technology Branch
Reentry Technology Division
Advanced Ballistic Reentry Systems

FOR THE COMMANDER

Nicholas C. Belmonte

NICHOLAS C. BELMONTE, Lt Col, USAF
Director, Reentry Technology Division
Advanced BALLISTIC Reentry Systems

UNCLASSIFIED

SECURITY CLASSIFICATION OF THIS PAGE (When Data Entered)

REPORT DOCUMENTATION PAGE		READ INSTRUCTIONS BEFORE COMPLETING FORM
1. REPORT NUMBER BMO TR-81-2	2. GOVT ACCESSION NO. AD-A108	3. RECIPIENT'S CATALOG NUMBER 847
4. TITLE (and Subtitle) "Performance Technology Program (PTP-S II): Vol. V Infrared Mapping of Boundary Layer Transition on a Slender Cone"		5. TYPE OF REPORT & PERIOD COVERED Final Report: 3/78 - 12/79
7. AUTHOR(s) A. Martellucci F. Makowski		6. PERFORMING ORG. REPORT NUMBER SAI-067-81R-010
9. PERFORMING ORGANIZATION NAME AND ADDRESS Science Applications, Inc. 994 Old Eagle School Road, Suite 1018 Wayne, Pennsylvania 19087		8. CONTRACT OR GRANT NUMBER(s) F04701-77-C-0126
11. CONTROLLING OFFICE NAME AND ADDRESS Ballistic Missile Office (BMO) Norton AFB, California		10. PROGRAM ELEMENT, PROJECT, TASK AREA & WORK UNIT NUMBERS
14. MONITORING AGENCY NAME & ADDRESS (if different from Controlling Office)		12. REPORT DATE April, 1980
		13. NUMBER OF PAGES 70
		15. SECURITY CLASS. (of this report) UNCLASSIFIED
		15a. DECLASSIFICATION/DOWNGRADING SCHEDULE
16. DISTRIBUTION STATEMENT (of this Report) Approved for Public Release; Distribution Unlimited. Distribution Statement 'A' of AFR 80-45 Applies.		
17. DISTRIBUTION STATEMENT (of the abstract entered in Block 20, if different from Report)		
18. SUPPLEMENTARY NOTES		
19. KEY WORDS (Continue on reverse side if necessary and identify by block number) Boundary Layer Transition, Hypersonic, Blunted Cone, Roughness, Angle-of- Attack		
20. ABSTRACT (Continue on reverse side if necessary and identify by block number) Surface heating was measured and boundary layer transition locations were deduced on a 7° half-angle cone model with a base diameter of 12.3". The tests were performed at Mach 8 in Tunnel B of the vonKarman Test Facility at Arnold Engineering Development Center. The objective of the current effort was to ex- perimentally define transition onset, zone extent and shape for configurations with (a) preshaped noses, (b) roughness patches simulating antenna windows, (c) steps due to misaligned frusta, and (d) biconic frusta. The model was made of an epoxy material whose insulating and emissive properties facilitated		

DD FORM 1 JAN 73 1473 EDITION OF 1 NOV 65 IS OBSOLETE

UNCLASSIFIED

(over)

SECURITY CLASSIFICATION OF THIS PAGE (When Data Entered)

UNCLASSIFIED

SECURITY CLASSIFICATION OF THIS PAGE(When Data Entered)

data acquisition through the VKF infrared scanning camera. The IR data was digitized and converted to surface temperature values by means of an equation derived from the basic laws of radiation. Local heat transfer rates were then deduced from the temperature data under the assumption that the model's surface temperature history was that of a homogeneous, semi-infinite slab subjected to a constant heat transfer coefficient. Comparisons of transition onset and end deduced from the IR system data are shown to compare favorably with data deduced from models instrumented with thermocouples or gardon heat gages.

ii. UNCLASSIFIED

SECURITY CLASSIFICATION OF THIS PAGE(When Data Entered)

TABLE OF CONTENTS

	<u>Page</u>
ABSTRACT (DD 1473)	1
LIST OF FIGURES	2
NOMENCLATURE	4
ACKNOWLEDGEMENTS	6
1.0 INTRODUCTION	7
1.1 Problem Definition	7
1.2 Test Objectives	8
1.3 Technical Approach	9
2.0 INFRARED SYSTEM	10
3.0 TEST FACILITY AND MODEL DETAILS	11
3.1 Test Facility	11
3.2 Model Data	11
4.0 SUMMARY OF DATA OBTAINED	18
5.0 DISCUSSION OF RESULTS	23
5.1 Spherical Nose Bluntness Effects	23
5.2 Nose Shape Effects	32
5.3 Frustum Roughness Patch Effects	37
5.4 Frusta Offset Effects	44
5.5 Bicone Configuration Effects	44
6.0 SUMMARY AND CONCLUSIONS	52
REFERENCES	55
APPENDIX A- INFRARED SYSTEM	56

Accession For	
NTIS GRA&I	<input checked="" type="checkbox"/>
DTIC TAB	<input type="checkbox"/>
Unannounced	<input type="checkbox"/>
Justification	
By _____	
Distribution/	
Availability Codes	
Dist	Avail and/or Special
A	

DTIC
ELECTE
S **D**
DEC 28 1981
D

LIST OF FIGURES

<u>No.</u>	<u>Title</u>	<u>Page</u>
1	Model Configuration Details	13
2	Model Nosetip Configurations	14
3	Misaligned Frusta Configuration	15
4	Model Installation Defining IR Field of View	17
5	Typical Isotherm Plot	19
6	Representative Centerline IR Data Plots with Definition of Transition Onset and End	24
7	Reproduction of the Color IR Photographs Depicting the Effect of Nose Bluntness and Shape on Transition	26
8	Effect of Nosetip Shape on the Surface Heating Distribution/Transition Zone	27
9	Comparison of the Transition Onset and End Locations - Current Data with that of Reference	28
10	Local Transition Reynolds Number Variation with Bluntness	29
11	Variation of Wind/Lee Transition Front Location on Blunted Cones with Angle of Attack	31
12	Effect of Nose Shape on Center of Pressure Location - Variation with Mach Number	33
13	Effect of Nose Shape on Center of Pressure Location - Variation with Bluntness	34
14	Transition Skewness as Affected by Nose Shape	36
15	Reproduction of the Color IR Photographs Depicting the Effect of a Roughness Patch on Transition	38
16	Effect of a Roughness Patch on the Surface Heating Distribution/Transition Zone	39
17	Reproduction of the Color IR Photographs Depicting the Effect of a Roughness Patch on Transition	40
18	Effect of a Roughness Patch on the Surface Heating Distribution/Transition Zone	41
19	Frusta Roughness Patch Effects on Transition Onset	43

LIST OF FIGURES (Cont'd.)

<u>No.</u>	<u>Title</u>	<u>Page</u>
20	Reproduction of the Color IR Photographs Depicting the Effect of Frusta Offset (Aft Facing) on Transition .	45
21	Effect of Aft Facing Frusta Offset on the Surface Heating Distribution/Transition Zone	46
22	Frusta Offset Effects on Transition Onset (Aft Facing)	47
23	Comparison of Aero Characteristics-Cones and Biconics	48
24	Center of Pressure Variation with Mach Number	50
25	Effect of Bicone Geometry on Transition Onset ($M_{\infty} = 8$)	51

NOMENCLATURE

A_B	Model Base area
C_p	Specific heat of model material
c	Velocity of light
D_B	Model base diameter
h	Heat transfer coefficient, $\dot{q} (T_{aw} - T_w)$
H	Planck's constant
H_0	Stagnation enthalpy
H_w	Air enthalpy based on T_w
k	Thermal conductivity of model material
K	Boltzmann's constant
L	Model length
M_∞	Freestream Mach number
P_∞	Freestream pressure
P_{t2}	Stagnation pressure downstream of a normal shock wave
\dot{q}	Heat transfer rate
q_∞	Freestream dynamic pressure
r	Body radius at the nosetip juncture
R_B	Model base radius
Re	Reynolds number
St_0	Wetted length from stagnation point to transition onset
St_∞	Stanton number based on freestream properties
T	Absolute temperature
T_i	Model initial temperature
T_0	Stagnation temperature

T_w	Wall temperature
Δt	Time measured from model insertion into flow
V_∞	Freestream velocity
W	Total radiant energy emitted from an object's surface per unit area and time
$W_{\lambda b}$	Blackbody spectral radiant emittance within a spectral interval one micrometer wide at wavelength λ
x	Axial distance measured from the apex of the sharp 70° half angle cone

GREEK SYMBOLS

α	Angle of attack
β	Term defined in Equation A-(5)
ϵ	Emissivity
λ	Wavelength
μ	Air viscosity
ρ	Model material density
ρ_∞	Freestream density
σ	Stefan-Boltzmann constant

ACKNOWLEDGEMENTS

This research was sponsored by the Space and Missile Systems Organization (SAMSO) of the Air Force Systems Command. Capt. R. Chambers was the project officer. The technical contributions of D. E. Boylan, R. Mathews, and the test support staff at ARO Inc./AEDC Division are gratefully acknowledged.

1.0 INTRODUCTION

1.1 Problem Definition

The targeting accuracy and reliability of a ballistic reentry vehicle (BRV) is a complex and interactive function of the geometric shape and design properties, the thermal environment, the nosetip and frustum materials' response to the thermal environment, and the coupled aerodynamic behavior of the "ablating" vehicle. Accuracy is also dependent upon manufacturing and assembly reliability and repeatability as it affects the center of gravity offset, lack of the uniformity in material properties, mismatch of the various frustum sections (i.e., steps and gaps), and several other factors. The interrelationship of these factors in achieving an acceptably small circular error probability (CEP) of impacting a target, although known qualitatively, are not entirely understood quantitatively.

At present one of the largest contributors to BRV entry dispersion is the lift perturbation produced by asymmetric boundary layer transition. Although the gross effects of asymmetric transition are fairly well known qualitatively, there is a need to develop a means of predicting more accurately the dynamic behavior of future vehicles during transition so that dynamic perturbations can be minimized through proper design. There is also a need to acquire an improved definition of the problem in terms of dispersion sensitivity to transition effects.

A principal element in reducing the transition dispersion contribution, especially for future systems, is in defining and understanding the causal mechanisms. A review of previous work has identified those physical mechanisms that could potentially produce aerodynamic stability degradation during boundary layer transition. One prominent mechanism is the progression of an asymmetrical transition front over the vehicle due to wind and body fixed sources. The motion disturbances associated with this source create an imbalance in the induced pressures and viscous forces. This can give rise to "in-plane" (or wind fixed) force and moment non-linearities and perturbations, and to "out-of-plane" forces and moments. The out-of-plane effects are generally thought of as being body fixed due to geometric asymmetries caused by antenna windows or nonsymmetric steps and gaps which give rise to asymmetric transition and impulsive out-of-plane loads.

In addition vehicle packaging and performance studies have shown that RVs with biconic frusta or with preshaped (i.e., non-spherical) noses may have some performance advantages over sphere cones. Furthermore, flight test results have shown that large changes in BRV stability occur during reentry that could, in part, be attributed to the nosetip shape change. This therefore suggests that if one could design a nosetip that nominally retains its preshape during reentry, increased high altitude stability could result with no weight penalty and with little if any effect on the low altitude characteristics of the vehicle.

However, little if any data exists relative to the transition performance of vehicles with the nosetip shapes that were considered here. The potential improvement in the aerodynamic performance could be offset by degraded "transition performance." That is, the altitude of transition onset, the sensitivity of the transition zone shape to angle of attack, and its rate of forward progression could be affected in a manner that would negate the improved aero performance. As a result, data were to be obtained to explore the relative effect of transition on vehicles with non-spherical noses versus those with spherical noses.

1.2 Test Objectives

The objective of the current effort was to experimentally define transition onset, zone extent and shape, and spread angle, for configurations with:

- a. preshaped noses,
- b. roughness patches simulating antenna windows,
- c. steps due to misaligned frusta,
- d. biconic frusta.

Tests were conducted at the vonKarman Test Facility at AEDC in Tunnel B at Mach 8.

1.3 Technical Approach

Aerodynamic heat-transfer data acquisition techniques can be categorized into two general methods: (1) those which provide discrete localized measurements, and (2) those which provide a map of the surface thermal conditions. Discrete measurement techniques usually require thermocouple or heat-gage instrumentation which yield output signals easily processed for data reduction by computers. However, only a limited number of thermocouples or gages can normally be accommodated by the model or test facility. Most thermal mapping procedures use coatings which change phase or radiance when heated. These coating techniques can provide immediate qualitative results, but lengthy off-line photographic data reduction procedures are required to obtain quantitative results. In addition, when phase-change paint coatings are used, the model must be cleaned and repainted between runs. Infrared scanning systems have the potential of combining the coverage of the mapping techniques with the computerized data reduction of the discrete measurement methods. Since models used for IR testing do not require internal instrumentation, configuration changes can readily be facilitated during the test cycle. The test model used in this investigation was 50 inches long, and was manufactured at Lockheed Huntsville using the proprietary epoxy material "LH." This material has a sufficiently high emissivity in the bandwidth of interest to be used as an infrared test model.

2.0 INFRARED SYSTEM

An infrared system has been under development within the von Karman Facility at the AEDC for several years (Refs. 1 and 2); recent developments of the system were described at the AIAA 10th Testing Conference (Ref. 3). Since that time, significant progress has been made in reaching the goal of combining both thermal mapping data and on-line digitizing of full frame (a maximum of 7700 discrete data points) infrared scans.

It is not the purpose of this paper to present a complete description of the total system. Rather, the reader should refer to information contained in Refs. 1-3 for details of basic concepts, system components, and data reduction techniques. Contained in Appendix A of this report is a discussion of the IR system and its utility in resolving a particular technology problem along with examples of computer generated isotherm and digital data plots are shown using results from this study.

3.0 TEST FACILITY AND MODEL DETAILS

3.1 Test Facility

Tunnel B is a closed circuit hypersonic wind tunnel with a 50-in. diameter test section. Two axisymmetric contoured nozzles are available to provide Mach numbers of 6 and 8 and the tunnel may be operated continuously over a range of pressure levels from 20 to 300 psia at Mach number 6, and 50 to 900 psia at Mach number 8, with air supplied by the VKF main compressor plant. Stagnation temperatures sufficient to avoid air liquefaction in the test section (up to 1350°R) are obtained through the use of a natural gas fired combustion heater. The entire tunnel (throat, nozzle, test section, and diffuser) is cooled by integral, external water jackets. The tunnel is equipped with a model injection system, which allows removal of the model from the test section while the tunnel remains in operation.

3.2 Model Data

A model that is to be used with the AEDC IR system in Tunnel B must have specific characteristics to accurately determine the surface temperature and the corresponding heat transfer to the model surface. Specifically, the material for that part of the model from which IR data are to be obtained must be:

- a. a good insulator and therefore have low thermal diffusivity;
- b. castable and machinable;
- c. a good radiator in the IR region of the spectrum at which the detector is sensitive;
- d. able to be repeatably exposed to high; temperature (up to 500°F) with no surface deterioration;
- e. able to withstand the aerodynamics loads of tunnel entry and exit;
- f. able to be manufactured in a large enough size for suitable boundary layer transition tests on blunt bodies.

The Lockheed Epoxy Material LH has these properties, is economical to fabricate, and was therefore used for the current study.

The model used in this test was basically a slender cone, with a 7-degree half-angle and a base diameter of 12.28 inches; the model wall was approximately one-half inch thick. It was built in several sections to allow different geometries to be assembled. The basic sharp 7-degree cone configuration, seen in Figure 1, was 50 inches long, and model stations were measured from the apex of this configuration. Details of the model components are shown in Figure 2. Through various combinations of the three forecones, eight nosetips, and ten nosecaps, a large number of conic and frustum biconic configurations with a variety of nose shapes could be assembled.

All of the model nosetips were made of steel to withstand the severe thermal environment in the nose region.

In addition to the nose shapes, two other geometry variables were included in the model design. At Model Station 20, the coupling between the aft cone and the forecone was constructed such that the joint could be assembled with a smooth surface, or with the forecone offset either 0.075-in. or 0.150-in. in the vertical plane (Figure 3). This provided a forward-facing step on one side of the model and a rearward-facing step on the other side. This was intended to simulate frustum section misalignment in the manufacturing of actual flight vehicles.

The final geometric variable was a series of roughness patches at Model Station 28. At this station the model was smooth in one quadrant while in the other three quadrants a rough area, approximately two inches square, was formed by bonding grit particles to the model surface. A different particle size was used for each patch, and the three sizes were 0.013-in., 0.030-in. and 0.060-in. (see Figure 1).

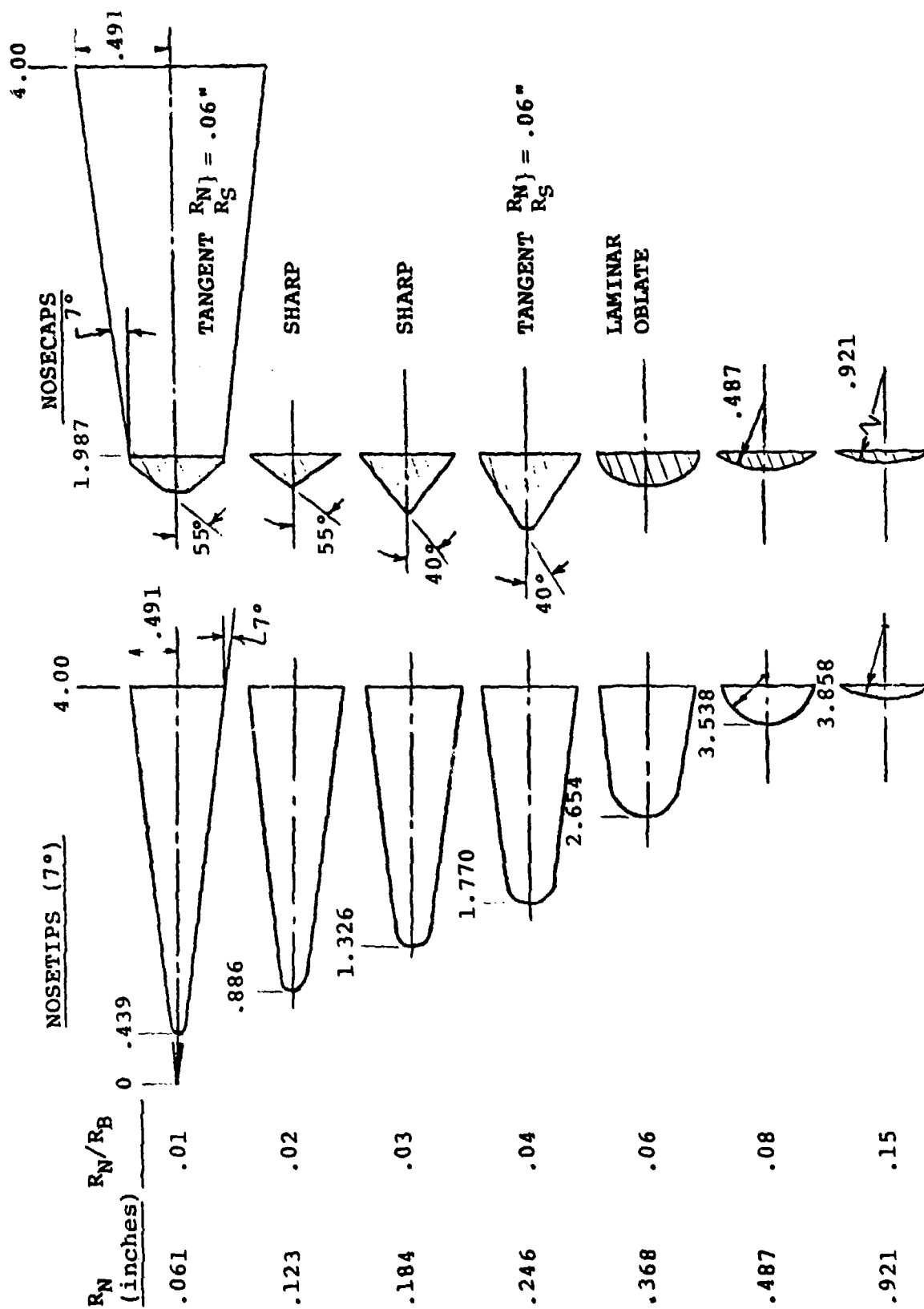
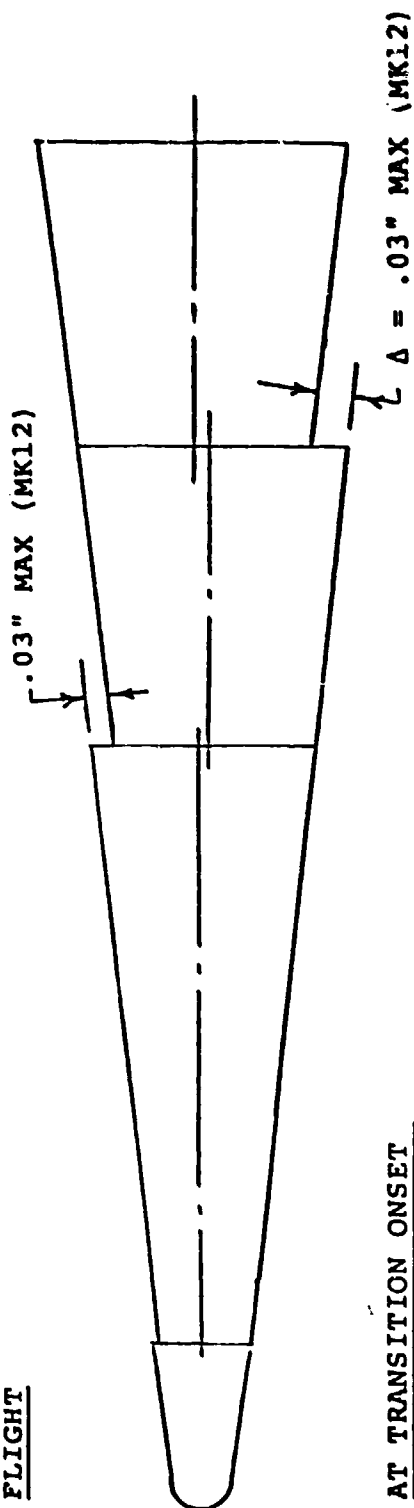


FIGURE 2. MODEL NOSETIP CONFIGURATIONS

FLIGHT



AT TRANSITION ONSET

$$\frac{\Delta}{\delta^*} = 1.0 \quad \frac{\Delta}{\theta} = 3.0$$

GROUND

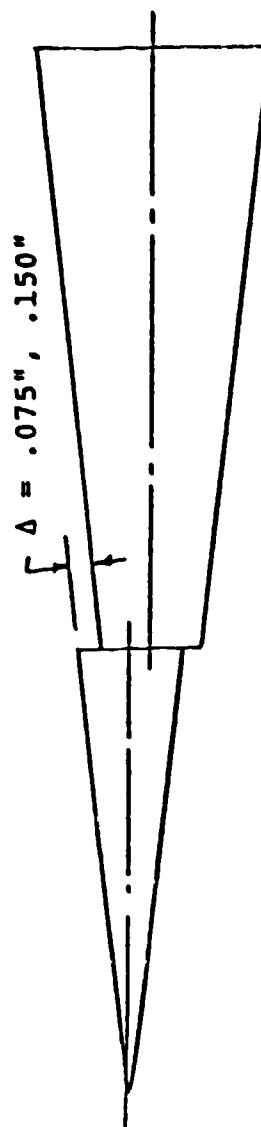


FIGURE 3. MISALIGNED FRUSTA CONFIGURATION

The model internal support structure was designed to attach either to a VKF six-component force balance or to a dummy balance. Installation in Tunnel B was as shown in Figure 4. It was mounted as far forward in the tunnel as was practical so the infrared camera could view the aft section of the model, where the boundary layer phenomena of interest were expected to occur. The appropriate IR camera field-of-view is indicated in Figure 4.

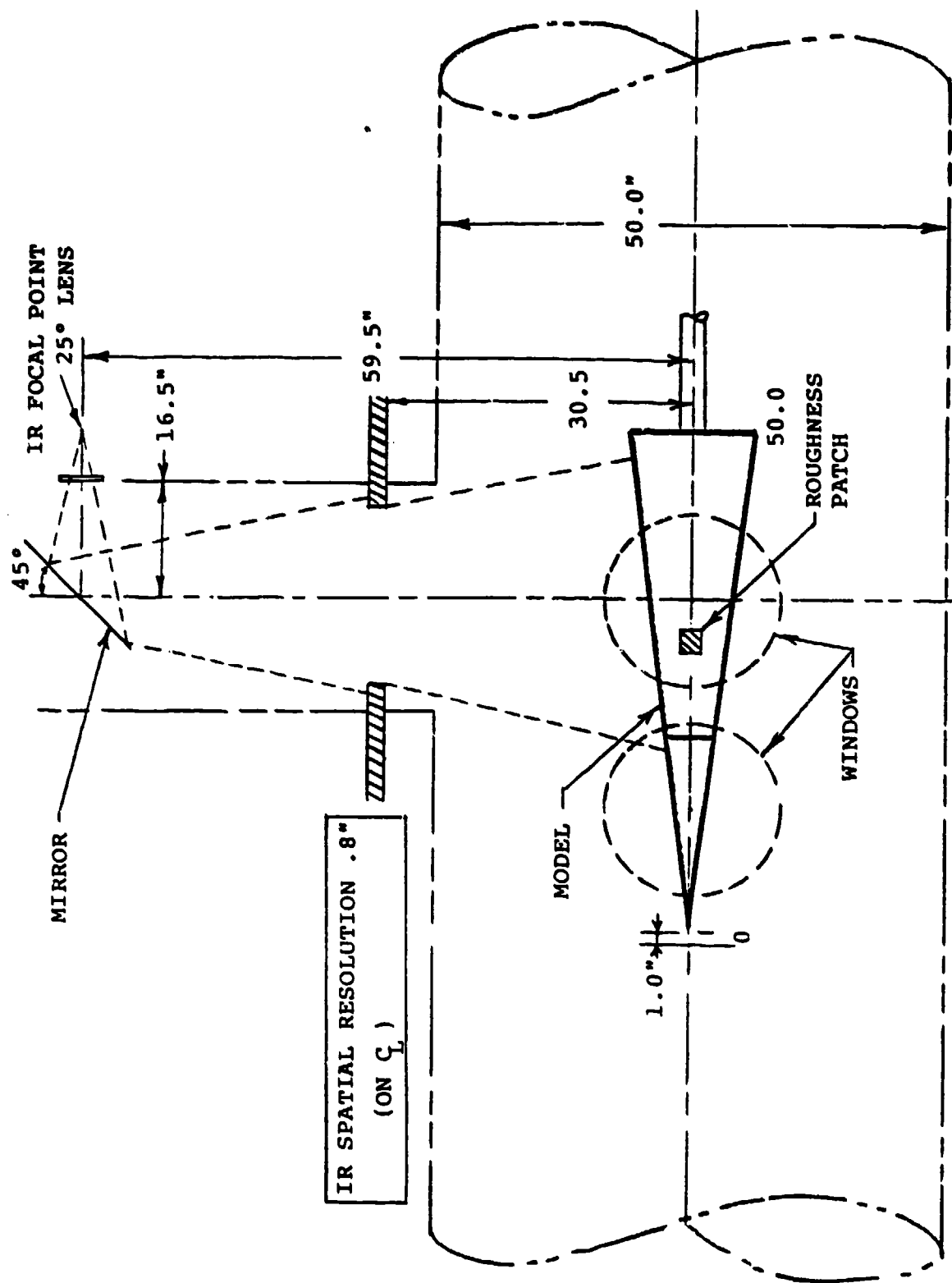


FIGURE 4. MODEL INSTALLATION DEFINING IR FIELD OF VIEW

4.0 SUMMARY OF DATA OBTAINED

The data generated with the AEDC IR system consists of:

- (1) A tabular listing of the tunnel freestream conditions, pertinent model information, local surface temperatures, and heat transfer coefficients. The surface temperature and heat transfer data are tabulated for each of the 2241 points in the IR field of view on the model surface,
 - (2) An isotherm map generated from the IR system output. This mapping technique uses the IR system output converted to a printer-plot format,
 - (3) Graphical presentation of the reduced data, such as the centerline heat transfer distribution displayed as a function of the axial coordinate,
- and
- (4) Camera coverage (color photographs of the IR video monitor) triggered at the time the data are digitized.

The data output from items (2) through (4) are available within minutes from the time the data were taken, thereby providing a useful tool for data diagnostics and test direction.

An example of an isotherm map is shown in Figure 5. In this map, each of the 40 symbols represents a temperature range of the IR output. The ranges do not overlap, so each of the data points are represented by one symbol and the printer displays the complete matrix. Both the computer plots and the color photographs are inherently qualitative in nature; however, they are useful for selecting the appropriate locations for which the primary tabulated data are plotted.

$$M_{\infty} = 8.0 \quad R_N/R_B = 0.03$$

$$Re_{\infty} = 3.8 \times 10^6 \text{ Ft}^{-1} \quad \alpha = 2^\circ \text{ (WINDWARD)}$$

$$k_S = 60 \text{ MILS}$$

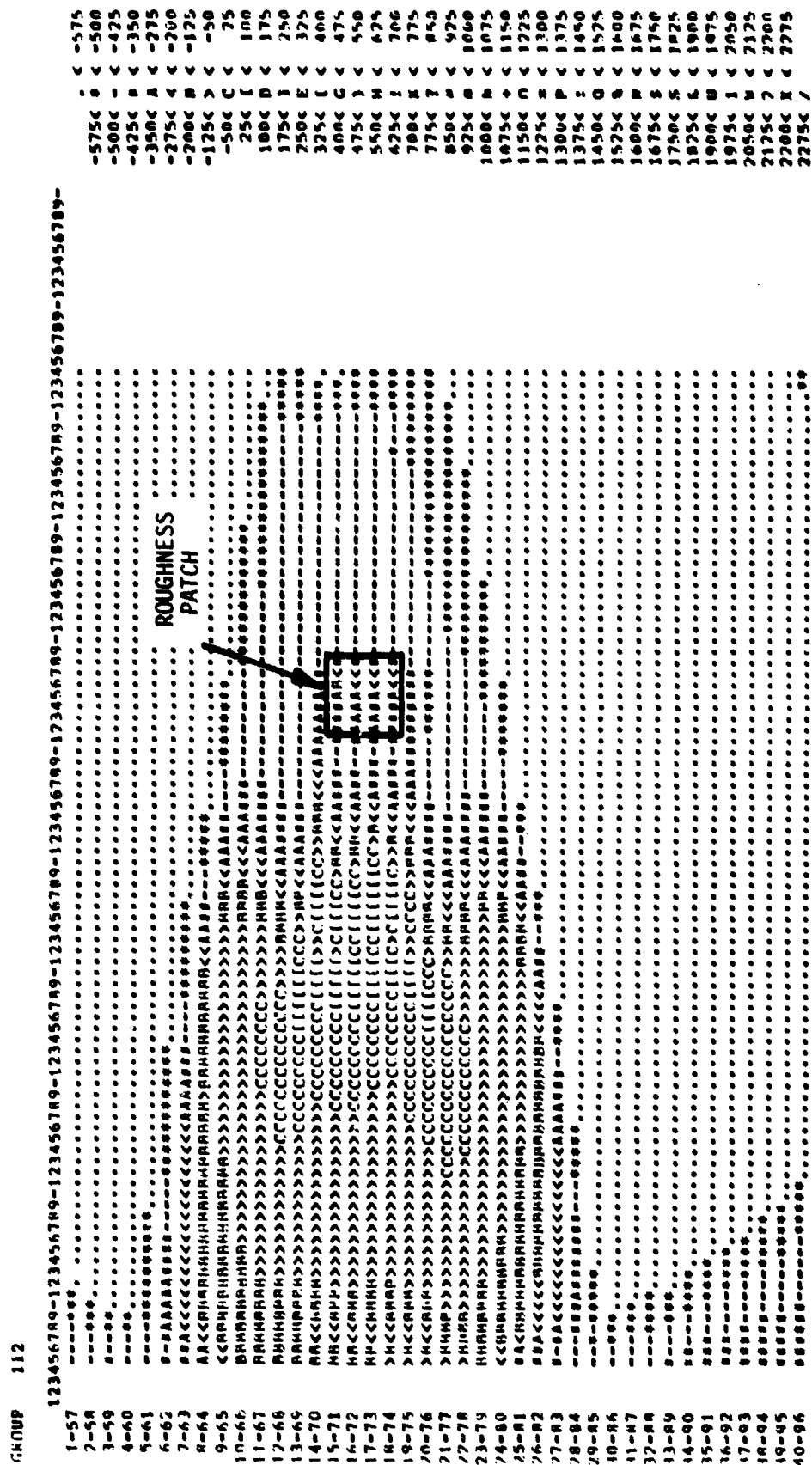


FIGURE 5. TYPICAL ISOTHERM PLOT

A listing of the IR data obtained during the current investigation is presented in Table 1. This table defines the freestream Reynolds number, the geometric configuration, and the angle of attack for which data were obtained. It should be noted that since data were obtained on the upper side of the model in the tunnel, a nose-up condition is defined as a plus (+) angle of attack and corresponds to leeward data. The converse is true for the windward side data.

TABLE 1. IR DATA SUMMARY

$M_\infty = 8, \theta_c = 7^\circ$ $(N/L)_{tr,0} / (N/L)_{tr,e}$ AT ANGLES OF ATTACK													
CONFIGURATION													
$Re_\infty \times 10^{-6} / \text{FT.}$	$O_{CF}, ^\circ$	R_N / R_B	MOSETIP SHAPE	$K_S, \text{IN.}$	$\Delta, \text{IN.}$	← WINDWARD →				← LEeward →			
						-2.0°	-1.0	-0.5°	-0.25	0°	0.25	0.5°	1.0°
1.3	7	0	--	0	0		.45/.74	--/.77	--/.70	.45/.68	.45/.67	--/.60	--/.49
		.01	SC	0	0		.45/.86			.45/.85			.45/.66
		.02	SC	0	0		.72/--			.72/--			.62/.85
		.03	SC	0	0		.76/--			.76/--			.75/--
		.04	SC	0	0					LAMINAR			
		.06	SC	0	0					LAMINAR			
		.08	SC	0	0					LAMINAR			
		0	--	0	0					LAMINAR			
		0	--	0	0					LAMINAR			
		0	--	0	0					LAMINAR			
		.01	SC	0	0					.71/.90			
		.01	SC	0	0					.76/--			
		.02	SC	0	0					.76/--			
		.02	SC	0	0					.78/--			
2.2		.02	SC	0	0					.67/.90			
		.02	SC	0	0					.64/.89			
		.02	SC	0	0					.63/.89			
		.01	SC	0	0					.61/.88			
		.01	SC	0	0					LAMINAR			
		.04	55T	0	0					LAMINAR			
		.04	LAM	.013	0					LAMINAR			
	10	0	--	0	0					.67/--			
		.04	55M	0	0					LAMINAR			
	13	0	--	0	0					.72/--			
				0	0					LAMINAR			
	7	.01	SC	0	0					--/.69			
		.02	SC	0	0					.56/.85			
		.01	SC	.060	0					--/.65			
	.02	SC	.013	0					.63/.89				
	.02	SC	.030	0					.62/.85				
	.02	SC	.060	0					.71/.90				
	.02	SC	0	0					.59/.78				
	.02	SC	0	0					.57/.80				
	0	--	--	0					.62/.87				

TABLE 1. IR DATA SUMMARY
 $M_w = 8, O_c = 7^\circ$

$Re_w \times 10^{-6}/FT.$	CONFIGURATION						$(N/L)_{tr_0} / (N/L)_{tr_e}$ AT ANGLES OF ATTACK						
	$\theta_{CF}, ^\circ$	R_H/R_0	MOSETIP SHAPE	$K_S, IN.$	$\Delta, IN.$	← WINDWARD				→ LEeward			
						-2.0°	-1.0	-0.5°	-0.25	0°	0.25	0.5°	1.0°
3.8	7	.01	SC	0	0	.55/.67	-.49			-.50			-.47
		.02	SC	0	0	.61/.78	.45/.63			.45/.71			.40/.63
		.03	SC	0	0	.62/.80	.61/.78			.69/.86			.49/.85
		.04	SC	0	0		.73/.89	.67/.84		.75/---		.50/.86	
		.06	SC	0	0		LAMINAR	.78/---	.77/---		.72/.91	.69/.90	
		.08	SC	0	0					LAMINAR			
		.03	SC	.013	0	.60/.75	.74/.86	.75/.90		.67/.89		.56/.81	.43/.57
		.03	SC	.030	0	.51/.79	.58/.76	.56/.80		.72/.90		.56/.83	.45/.88
		.03	SC	.060	0	.56/.68		.81/---		.68/.84		.56/.80	.45/.82
		.04	SC	.013	0			.79/---		.80/---		.71/.90	
		.04	SC	.030	0			.69/.78		.76/---		.65/.88	
		.04	SC	.060	0					.71/.88		.60/.85	
		.03	SC	0	-.150		.60/.72			.57/.73			-.70
		.04	SC	0	-.075		.72/.89			.72/.90			.49/.88
		.04	SC	0	-.150		.66/.80			.61/.80			-.89
		.04	55T	0	0					.76/---			.50/.85
10°	10°	.04	55N	0	0		.79/---			.74/---			.52/.85
		.04	40T	0	0					.71/.90			.46/.84
		.04	40N	0	0		.74/.80			.73/.90			.40/.63
		.04	LAM.	0	0		.74/.91			.77/---			.55/.88
		.04	.06N	0	0		.79/---			.74/---			.60/.56
		.04	55N	0	0		LAMINAR			.71/---			.70/---
		.04	40N	0	0		.76/---			.75/---			.66/.87
		0	--	0	0		-.50			TURB.			
		0	40N	0	0		.74/---			.75/---			.66/.90
		.04	40N	0	0								

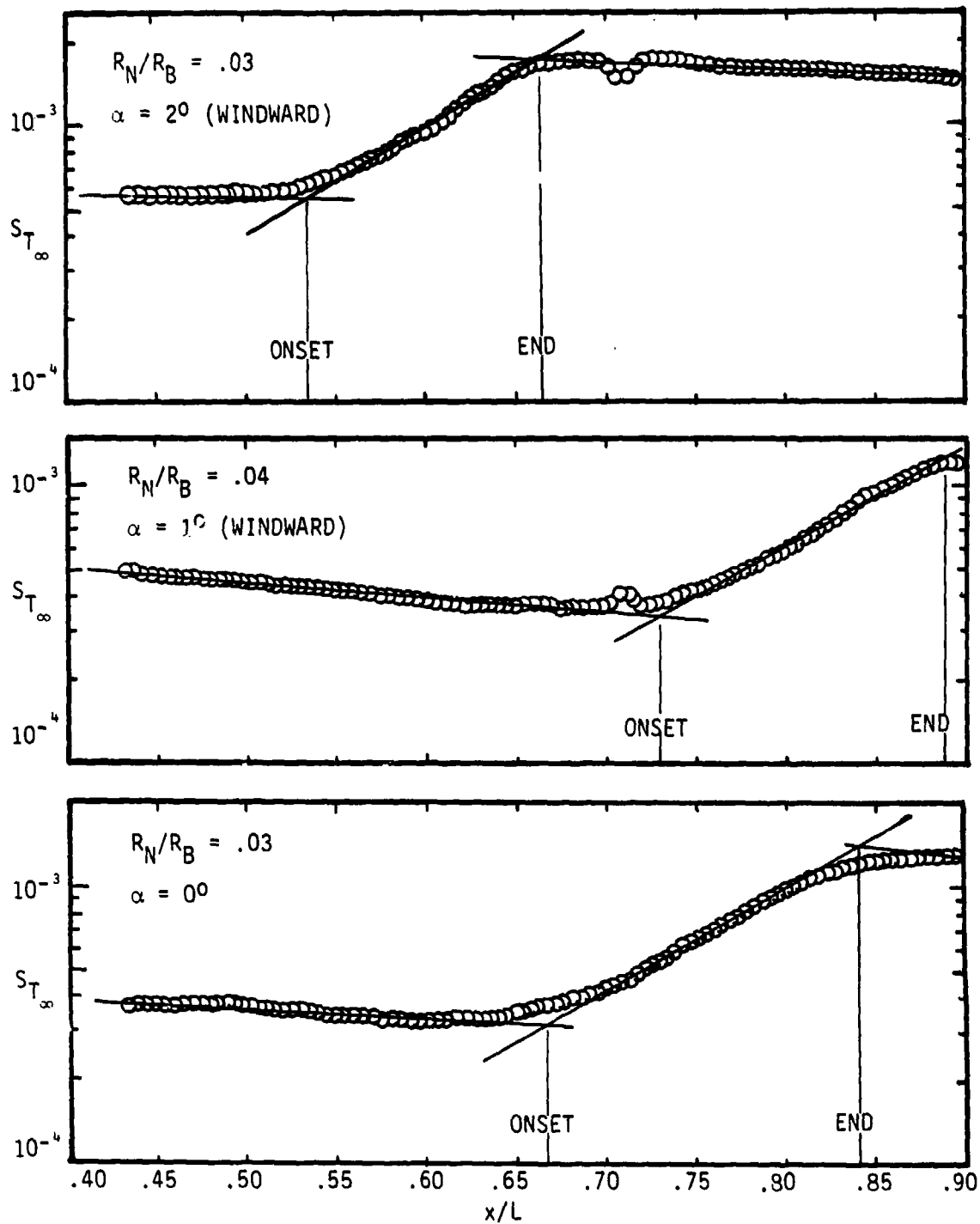
5.0 DISCUSSION OF RESULTS

The data obtained in the current study is summarized in the AEDC technical report of Reference 4. Distribution of the detailed data tabulations is available from AEDC to qualified DoD contractors with BMO approval. Contained in this section is a description of the analysis procedure used to define the onset and end of transition and an interpretation of the results.

Digital data obtained from the IR system were plotted as a function of x/L along the model centerline. As noted in Figure 4, the IR camera's field of view extended from $x/L \approx .45$ to $x/L \approx 0.90$. Some samples of this plot are shown in Figure 6. The slight variation in the data at $x/L = 0.71$ is caused by a stripe of reflective paint which served as a reference marker. Also shown in Figure 6 is the straight line method which was consistently used in the current investigation to define the axial location of transition onset and end. It was decided that this approach would provide a consistent definition of the transition locations which are also compatible with published data. It is evident from Figure 6 that the onset of transition, defined as the first departure from the laminar heating, would occur at a slightly smaller value of x/L , and the end at a slightly larger value of x/L (each within 5% of the "linear" method). However the definition of the value determined from the minima and maxima is subjective, and it was decided that the linear method provided consistency. The values of transition onset and end listed in Table 1 summarizes all of the data obtained and are tabulated in terms of x/L (from the 7° cone apex).

5.1 Spherical Nose Bluntness Effects

The data obtained for the 7° cone with the spherically blunted noses were used as a basis for comparison with the shaped nose effects, and also a bridge for comparison with data obtained from instrumented models (thin skin thermocouples or heat transfer gages). Therefore prior to



$(M_\infty = 8, Re_\infty/Ft. = 3.8 \times 10^6, T_w/T_0 = 0.4)$

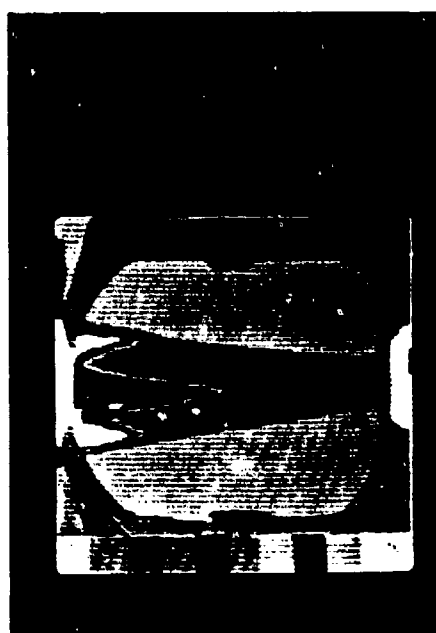
FIGURE 6. REPRESENTATIVE CENTERLINE IR DATA PLOTS WITH DEFINITION OF TRANSITION ONSET AND END

discussing results pertinent to the primary objectives of this test the data for the spherically blunted cone will be presented first.

Infrared data were obtained on the basic 7° half angle cone for noses of varying spherical bluntness and for several non-spherical shapes. Shown in Figure 7 are black and white reproductions of the IR color photographs for some representative data depicting the influence of nose bluntness and shape on the leeside heating (temperature) pattern at a one degree angle of attack. It is evident from these photographs that the shape of the nose has an effect on the transition location and shape. Shown in Figure 8 are the deduced heat transfer distributions for the same data groups depicted in Figure 7. With transition onset and end defined as is shown in Figure 6, the influence of spherical bluntness on the location of the transition zone, as derived from the current data, is shown in Figure 9. Also shown in this figure are data from Martellucci and Neff⁵ obtained on a thin-skin, smooth-walled cone with $\theta_c = 7.2^\circ$ using backface thermocouples. These data were also obtained in the AEDC Tunnel B facility at Mach 8. The agreement between the two sets of data are excellent.

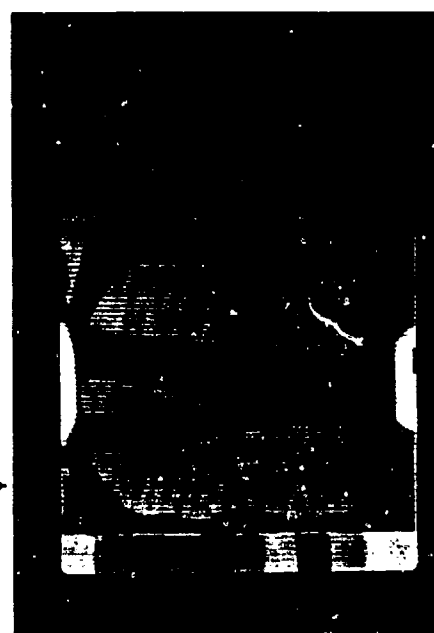
The data from the current series of tests were also compared to the bluntness data of Stetson and Rushton⁶ and Softley⁷, in terms of local wetted length Reynolds number to the transition onset point, Re_{ST} , versus the freestream Reynolds number based on nosetip radius (Figure 10). These data were obtained for Mach numbers in the range of 5.5 through 12.

The local viscous flow properties (i.e., Reynolds number, Mach number, etc.) were computed with the Blottner code⁶ which utilized the inviscid flow properties generated by Hall's code⁹. The data plotted in this format depicts the transition bluntness reversal first noted by Stetson and Rushton. On the "sharp" cone side of the curves (i.e., $Re_{\infty} \leq 10^5$), there is a trend of increasing transition Reynolds number, Re_{ST} , with Mach number. Interestingly, this trend is reversed on the blunt cone side.



SPHERE-CONES
 $\rightarrow R_N/R_B = 0.03$

$R_N/R_B = .04 \rightarrow$



$M_\infty = 8.0$
 $Re_\infty = 3.3 \times 10^6 \text{ Ft}^{-1}$
 $\alpha = 1^\circ \text{ (LEESIDE)}$



BICONE NOSETIPS
 $r/R_B = .04$
 $\rightarrow 40^\circ$

$55^\circ \rightarrow$

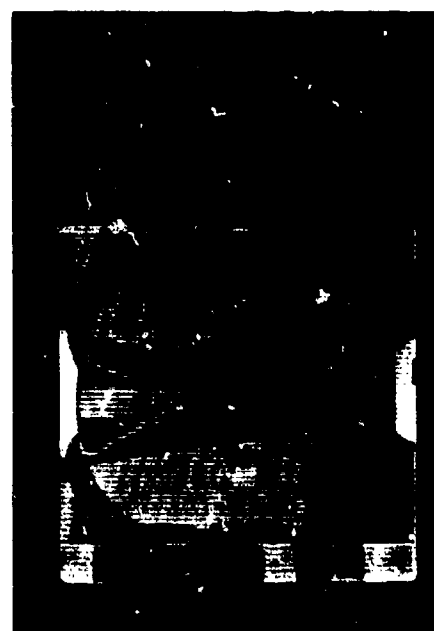


FIGURE 7. REPRODUCTION OF THE COLOR IR PHOTOGRAPHS DEPICTING THE EFFECT OF NOSE BLUNTNESS AND SHAPE ON TRANSITION

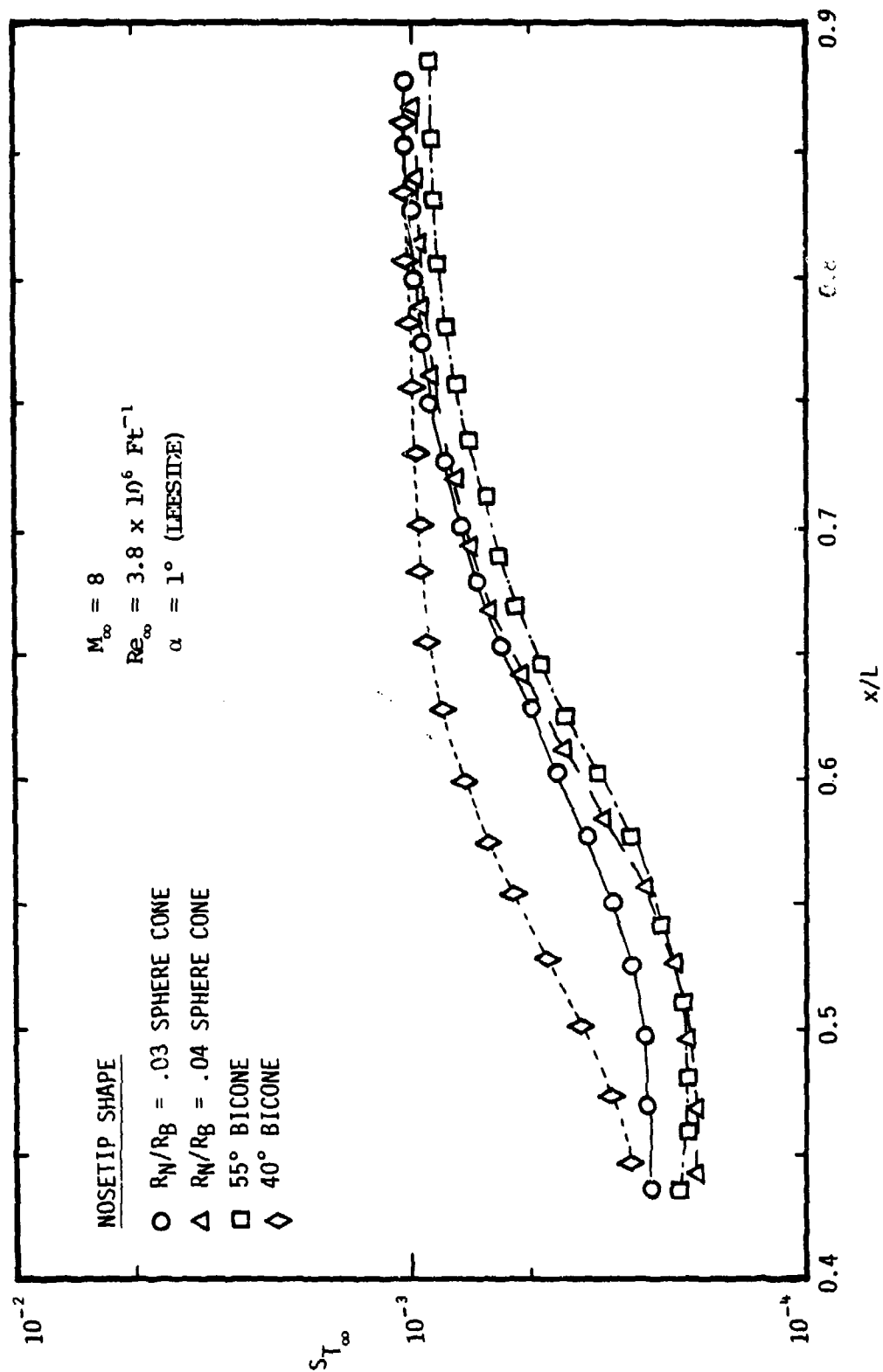


FIGURE 8 . EFFECT OF NOSETIP SHAPE ON THE SURFACE HEATING DISTRIBUTION/TRANSITION ZONE

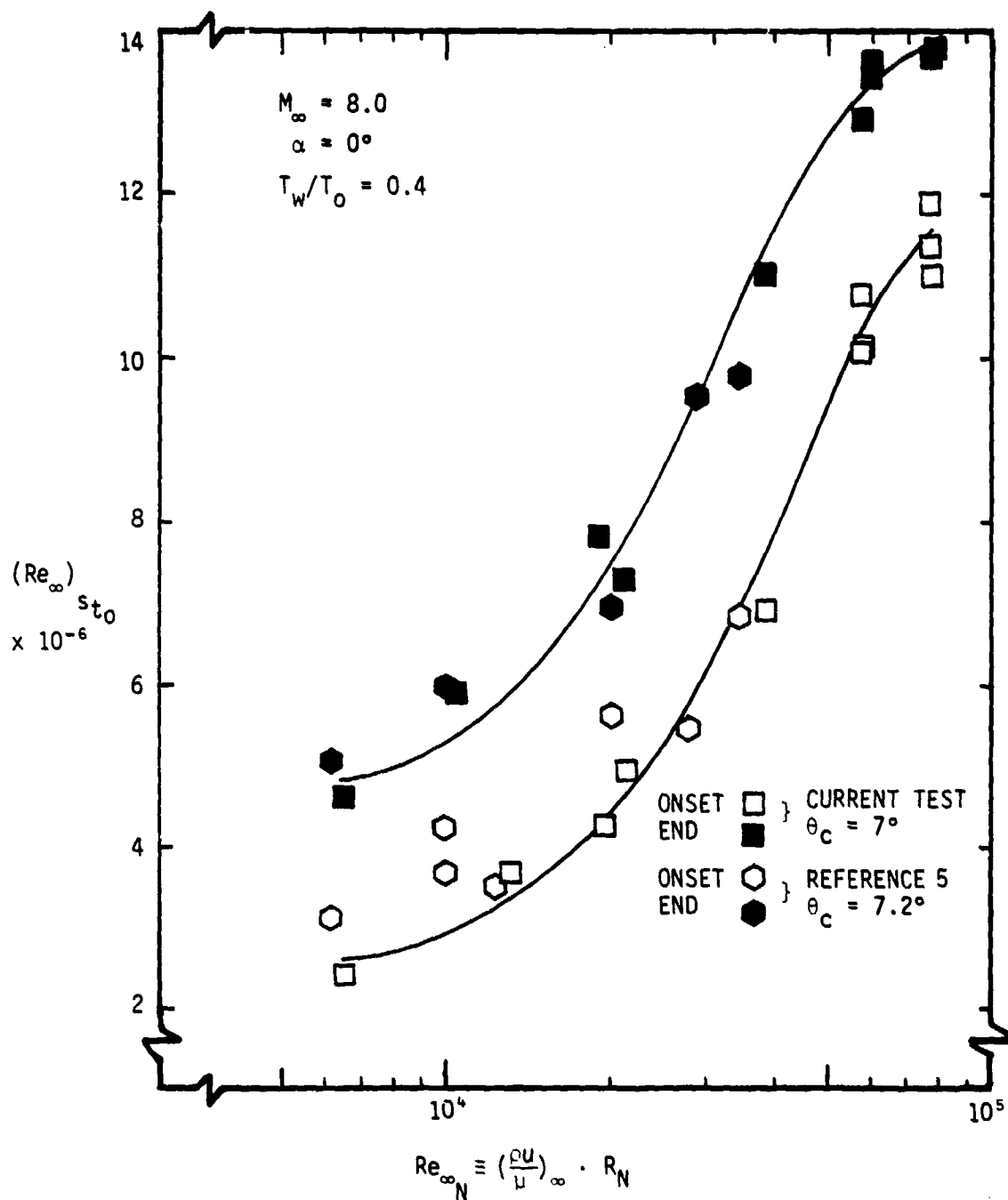


FIGURE 9. COMPARISON OF THE TRANSITION ONSET AND END LOCATIONS - CURRENT DATA WITH THAT OF REFERENCE

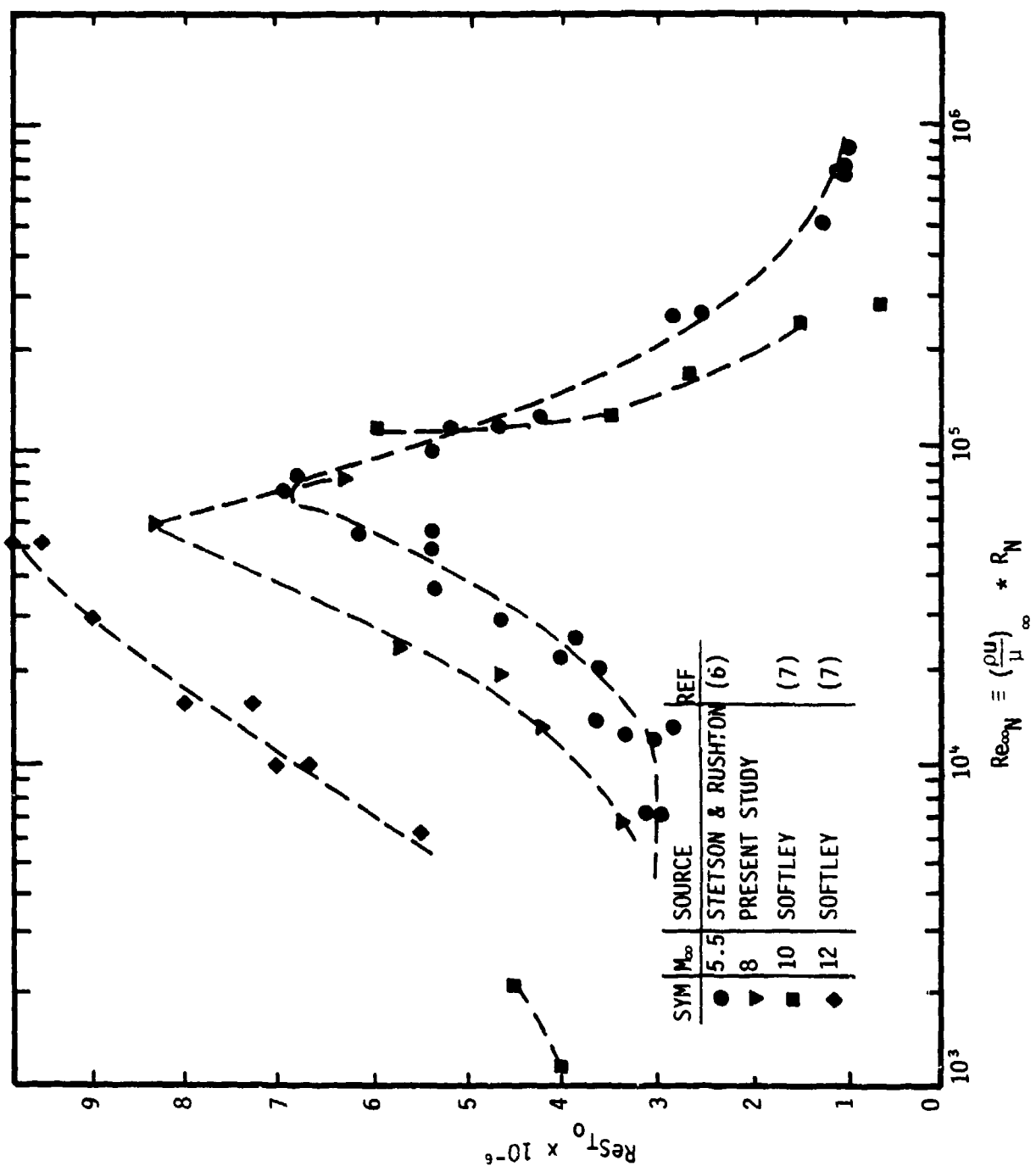
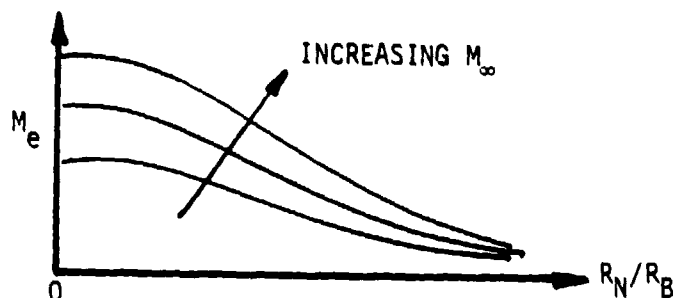


FIGURE 13. LOCAL TRANSITION REYNOLDS NUMBER VARIATION WITH BLUNTNESS

These trends can be attributed in part to the bluntness effects on local Mach number (i.e., entropy swallowing) as seen below:



For blunt cones, the local edge Mach number is quasi independent of free-stream Mach number therefore transition would be affected by other factors such as streamline stretching, entropy swallowing, etc. Nevertheless, it can be seen from Figure 10 that the data obtained with the IR system are consistent on a freestream Mach number basis with data from other sources.

The angle of attack influence of bluntness on transition skewness may be seen in Figure 11. In this figure the data from the current tests are displayed with the data of Stetson and Rushton⁶, Holden¹⁰, and Muir and Trujillo¹¹. Within the bluntness range tested in this series, the current data agree well with the other data sources. It is of interest to note that for nose bluntness ratios below 6%, transition is further forward on the leeside than on the windward side. The blunt cone data of Muir and Trujillo for $R_N/R_B = 0.32$ show the opposite trend. This bluntness reversal - wind to lee - has been observed by other experimenters as well.

The current data, obtained with the AEDC IR thermal data system, were seen to compare well with other data sources. Therefore, it is concluded that this data acquisition system can be employed with confidence. In the following sections, the influences of nose shape, roughness, etc. will be presented.

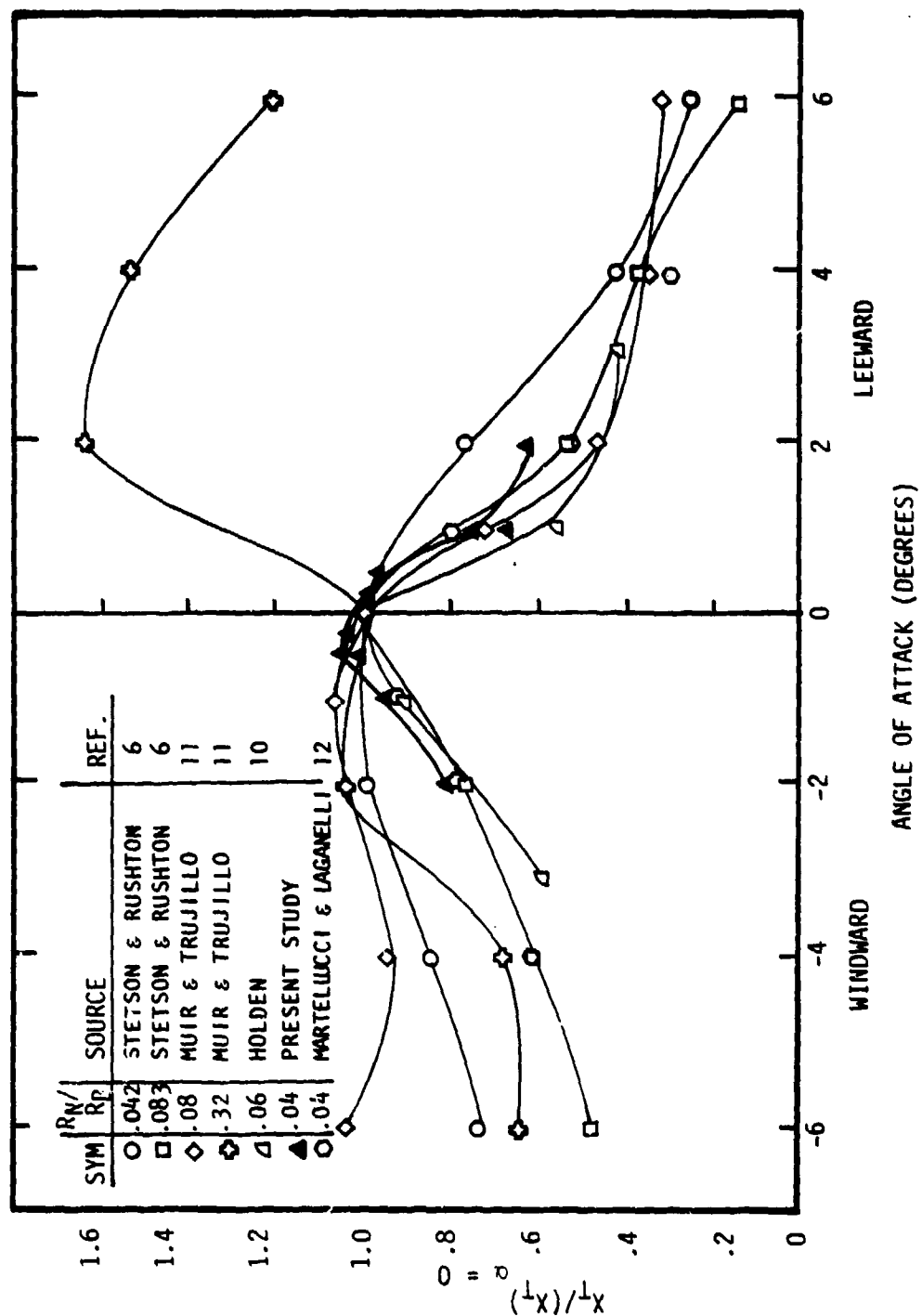


FIGURE 11. VARIATION OF WIND/LEE TRANSITION FRONT LOCATION ON PLUMED CONES WITH ANGLE OF ATTACK

5.2 Nose Shape Effects

Prior to presenting and discussing the data obtained for the configurations with the non-spherical noses, it would be advantageous to discuss why these configurations are of potential interest to ASMS (nee ABRES). Ballistic reentry vehicles with nosetip bluntness ratios of 5 to 12% and with bluff non-spherical noses were inherently more stable than those with spherical noses. The potential benefits that can be derived from nosetip preshaping are shown in Figures 12 and 13. The information presented in these figures was generated with the inviscid code of Reference 9. Figure 12 presents the location of the center of pressure versus Mach number for a vehicle with 10% bluntness for several nosetip shapes. Figure 13 presents the same results versus bluntness ratio at Mach 20. It is evident that significant stability increases can be realized with the bluff shapes (i.e., 55° bicone or ellipsoidal) as compared to the more slender (i.e., 40° bicone) nosetips. Increased stability is generally synonymous with decreased dispersion, thus this simple passive approach is but one method of favorably affecting vehicle design. The objective is to select a nosetip shape that provides high altitude benefits and retains the same nominal shape during reentry, thereby providing increased stability. One intent of the transition experiment of the current study is to evaluate the transition performance of vehicles with various nosetip preshapes to insure that no deleterious behavior is evident.

IR data were obtained on the 7° cone for each of the non-spherical nose configurations shown in Figure 2. Tests were conducted over an angle of attack range commensurate with typical BRV values at the transition onset altitude as shown in Table 1. Listed below is a summary of the data obtained at $\alpha = 0^\circ$ for $Re_\infty/Ft. = 3.8 \times 10^6$.

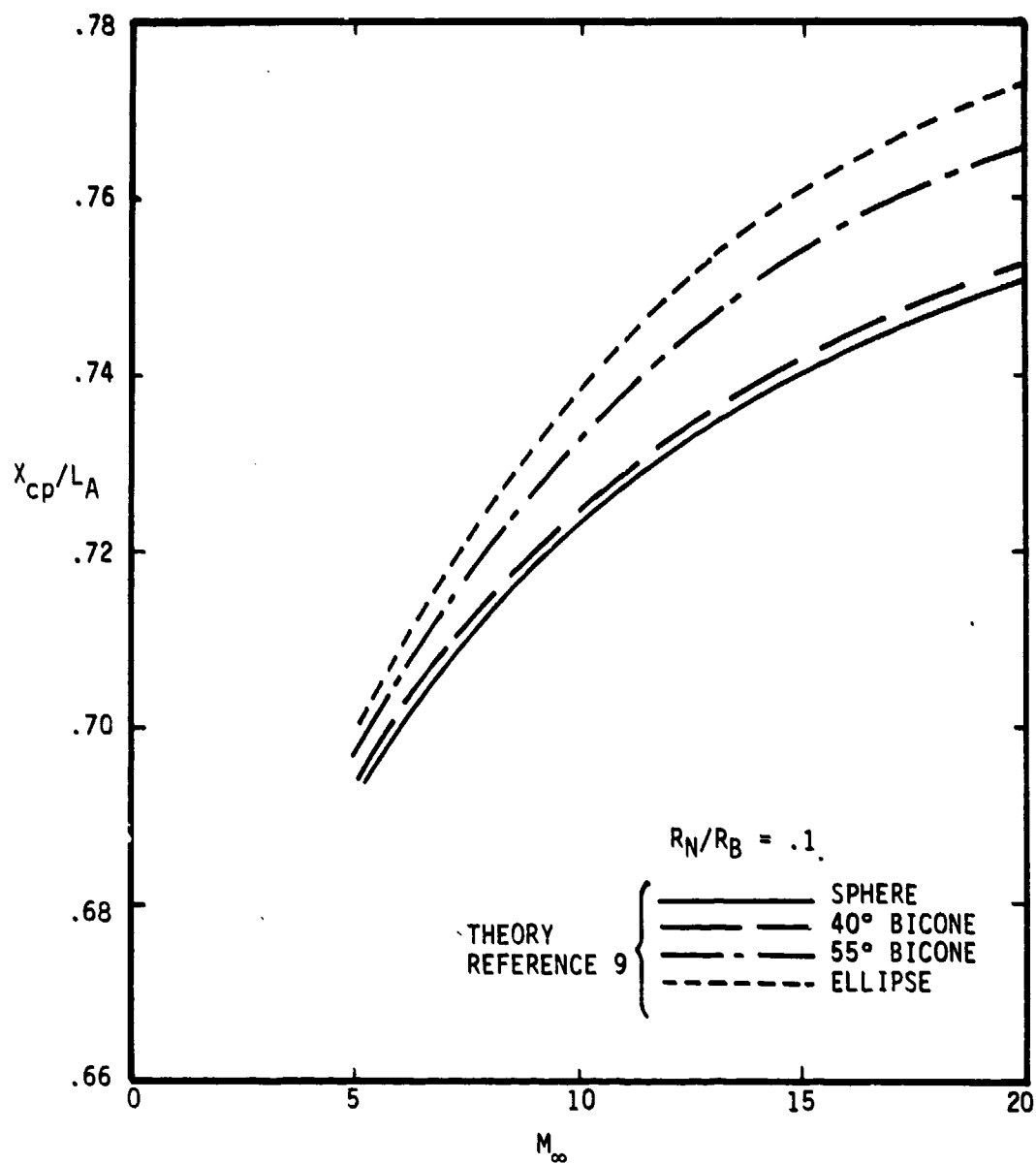


FIGURE 12. EFFECT OF NOSE SHAPE ON CENTER OF PRESSURE LOCATION - VARIATION WITH MACH NUMBER

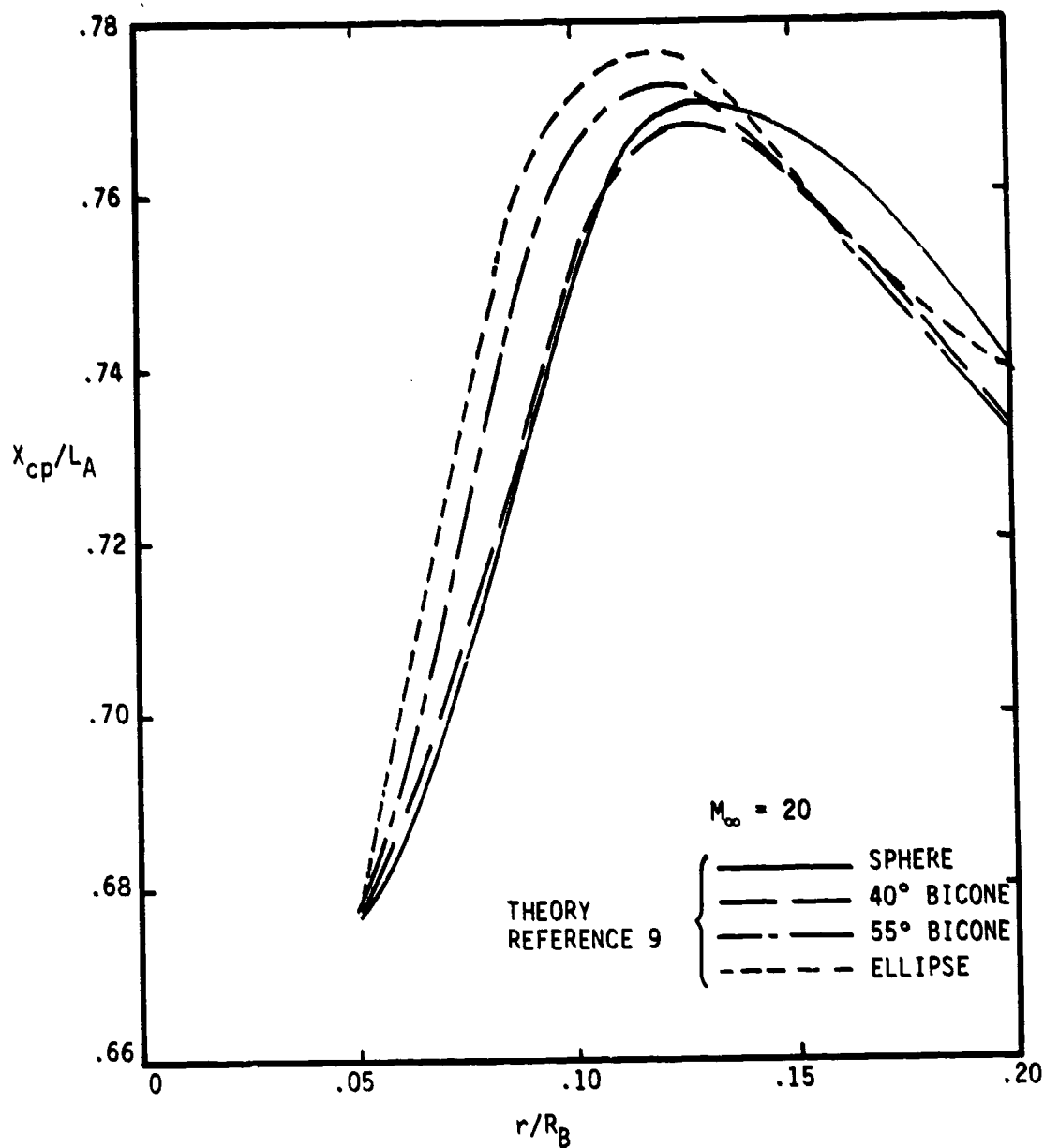


FIGURE 13. EFFECT OF NOSE SHAPE ON CENTER OF PRESSURE LOCATION - VARIATION WITH BLUNTNESS

Configuration ($r/R_B = .04$)	Axial Location of Transition Onset (x/L) _{tr₀}	Local Wetted Length Reynolds No. at Onset Re _{str₀}
Spherical Nose	0.75	5.7
Laminar Oblate (ellipsoidal)	0.77	5.5
55° Tangent	0.76	6.1
40° Tangent	0.71	5.4

One will note that the location of transition onset is slightly delayed for the bluff nose configurations (i.e., laminar and 55°T) compared to the spherical nose case, and slightly enhanced for the sharper nose configuration. Considering that nosetip ablation during reentry will result in an oblate nose shape, one therefore observes that the cone with the 55° nose has the same nominal transition performance as the laminar oblate blunted configuration.

One measure of the influence of transitional boundary layer flows on the targeting accuracy is related to the degree of skewness of the transition cone - wind to lee - evident at angle of attack. This is a consequence of the changes in viscous induced pressure and wall shear from laminar to turbulent flow. Shown in the bar chart of Figure 14 is a comparison of the degree of skewness observed for each of the noses tested at $\alpha = 1^\circ$. One notes from this figure that the bluffer noses (i.e., the laminar oblate and 55°) which are tangent to the air cone exhibit less transition skewness than the sharper nose (i.e., 40°). The non-tangent 40° and 55° noses exhibit more skewness than their tangent counterparts. It should be noted that the transition onset location for the non-tangent noses is nominally identical to the location for tangent shapes on the windward ray; however, it is further forward on the leeward ray. Obviously the sharp corner destabilizes the leeside boundary layer creating the greater skewness. Since reentry ablation will cause all sharp corners to increase in radius, it can be concluded that for the tangent geometries, bluffer nosed vehicles will have improved transition performance (i.e., less high altitude dispersion contribution to targeting accuracy) over sharper vehicles.

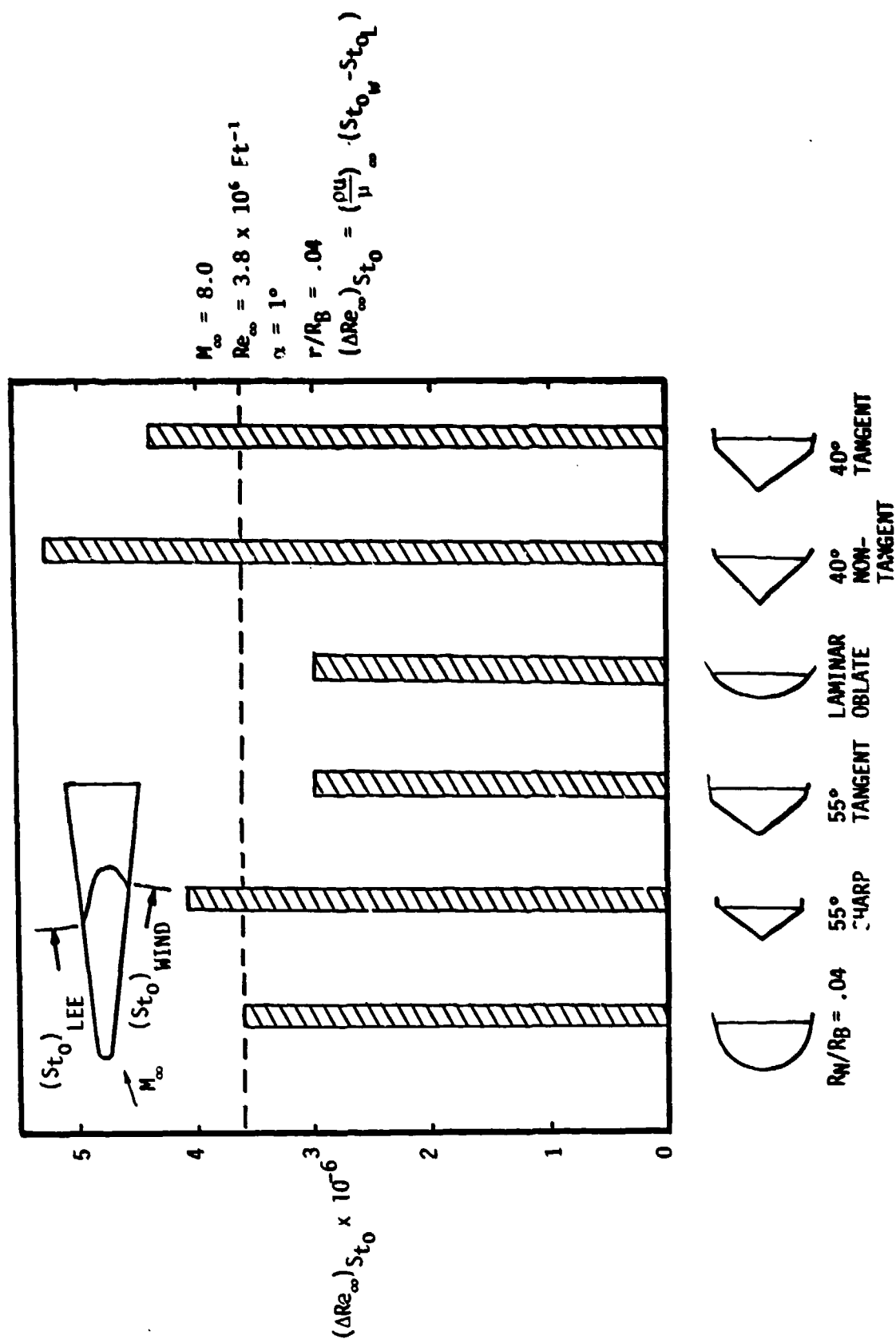
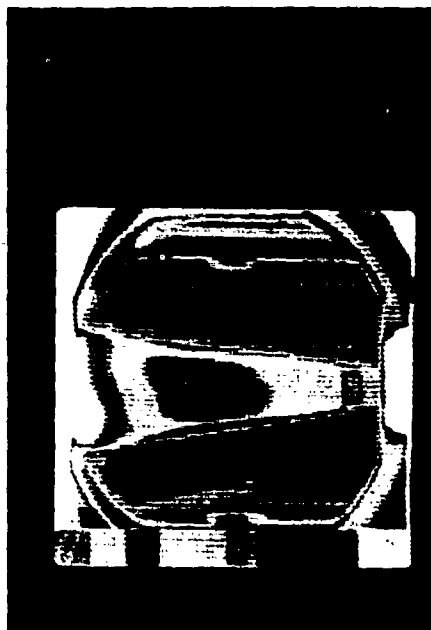


FIGURE 14. TRANSITION SKEWNESS AS AFFECTED BY NOSE SHAPE

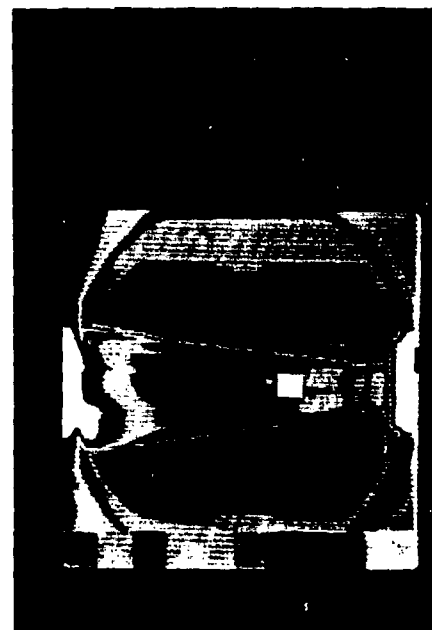
Relative to the primary goal of this subset of experiments, it can be concluded that the reentry performance of a BRV could be improved if the nose were preconfigured to be bluff, and whose material properties coupled to this preshape were such as to cause the shape during reentry to remain bluff. This conclusion should be verified by flight test.

5.3 Frustum Roughness Patch Effects

Reentry vehicles generally have antenna windows mounted in the frustum. The antenna window materials have sufficiently different ablation characteristics such that they start ablating at an altitude different from the shield, which, in general, also recedes at a different rate. As a consequence, they impose a disturbance to the flow which could affect the state of the boundary layer downstream of the window. Localized roughness patches were used in this study to simulate the disturbances associated with antenna windows. As defined in Section 3, the model was manufactured with three 2" x 2" roughness patches of different roughness height ($k_s = 13, 30, \text{ and } 60 \text{ mils}$) located 90° apart. Data were obtained with the model rotated so that, for a given model configuration, each patch was at top-dead-center (i.e., in the viewing range of the IR camera). IR measurements were made for several values of the Reynolds number, angle-of-attack, and nose bluntness. Shown in Figure 15 are black and white reproductions of the color IR photographs of the windward side ($\alpha = 0.5^\circ$) of the 4% blunt sphere cone. Figure 16 contains the inferred heat transfer distributions for the same cases. It is interesting to note that transition onset initially is delayed behind the roughness, moving from $x/L \approx 0.75$ for $k_s = 0$ to $x/L \approx 0.81$ for $k_s = 13 \text{ mils}$. Then as k_s increases further, transition onset moves forward. Another example of roughness delaying transition is visible from the photographs of Figure 17 and the attendant heat transfer distributions shown in Figure 18. In this case, transition onset for the smooth wall is located at $x/L = 0.58$ and as k_s increases



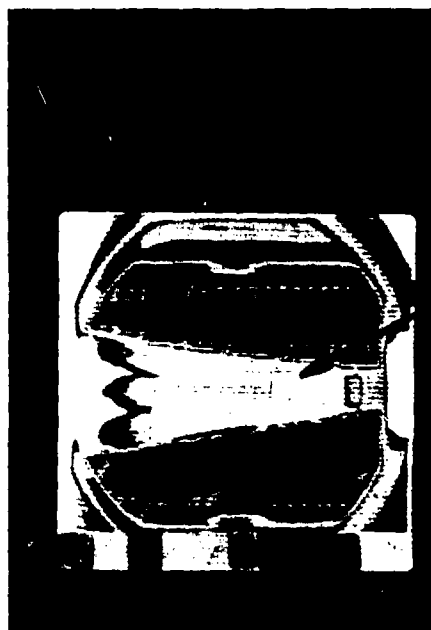
$k_s = 0$



$k_s = .013''$

$M_\infty = 8.0$
 $Re_\infty = 3.8 \times 10^6 \text{ Ft}^{-1}$
 $R_N/R_B = 0.04$
 $\alpha = 0.5^\circ \text{ (WINDWARD)}$

$k_s = .030''$



ROUGHNESS
 PATCH

$k_s = .060''$

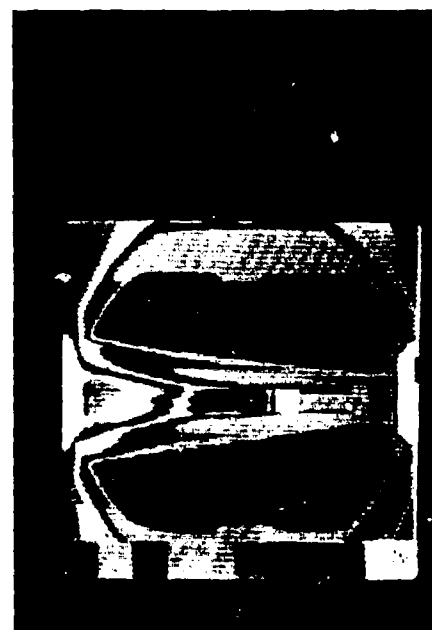


FIGURE 15. REPRODUCTION OF THE COLOR IR PHOTOGRAPHS DEPICTING THE EFFECT OF A ROUGHNESS PATCH ON TRANSITION

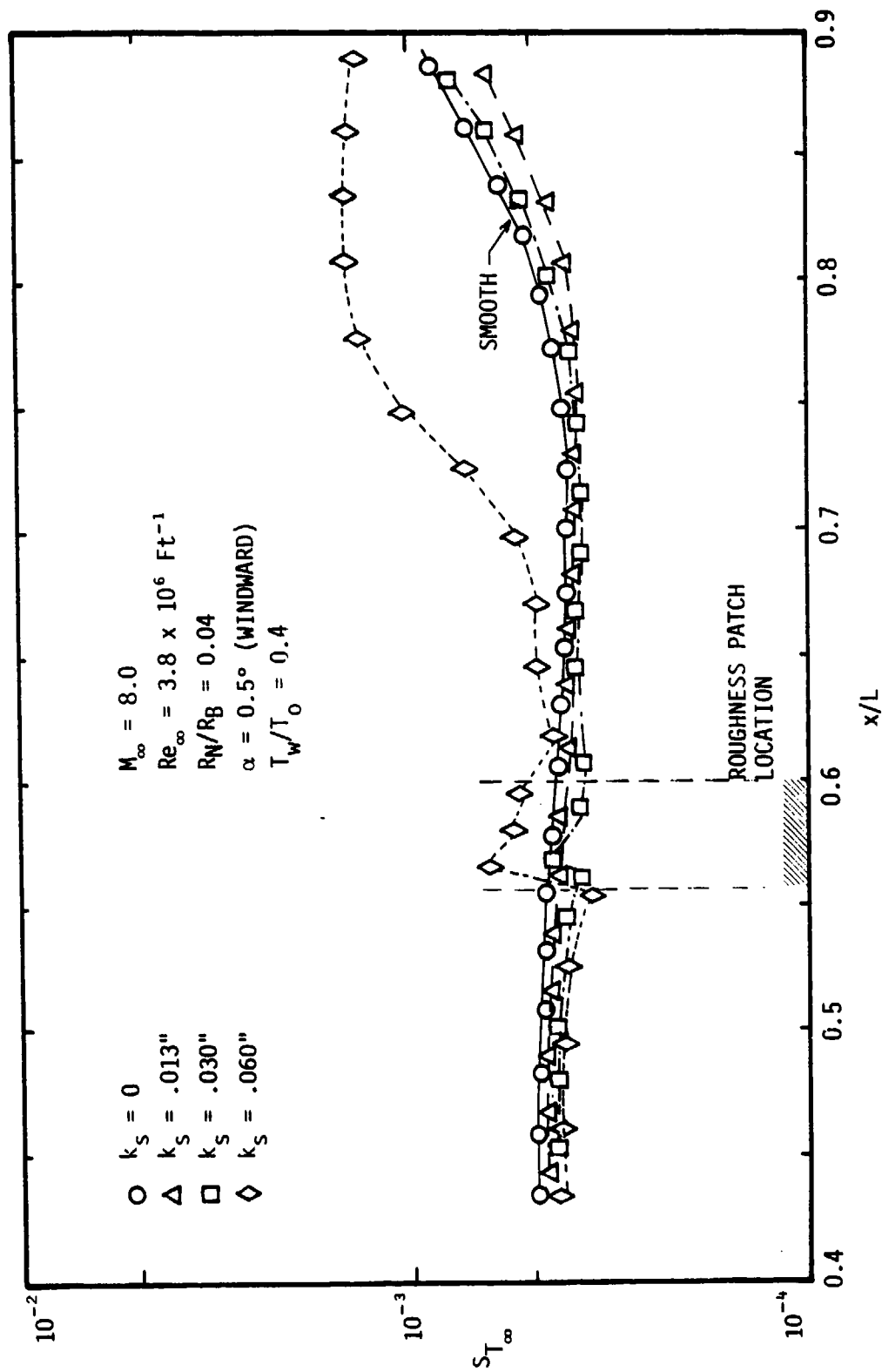
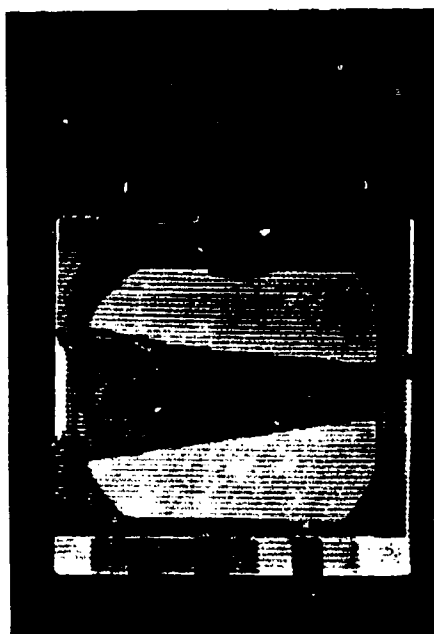
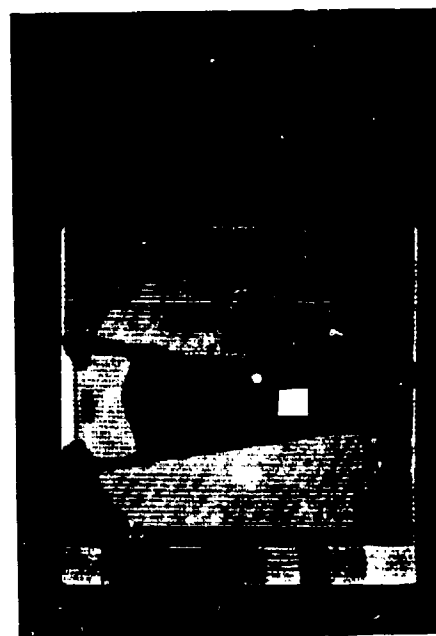


FIGURE 16. EFFECT OF A ROUGHNESS PATCH ON THE SURFACE HEATING DISTRIBUTION/TRANSITION ZONE



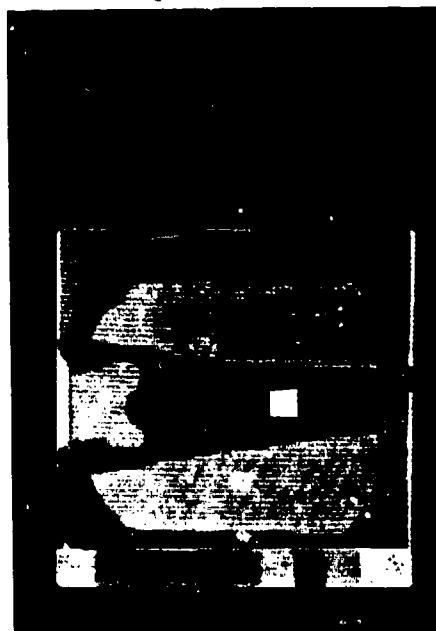
$k_s = 0$



$k_s = .013''$

$M_\infty = 8.0$
 $Re_\infty = 2.2 \times 10^6 \text{ Ft}^{-1}$
 $R_N/R_B = 0.02$
 $\alpha = 0^\circ$

$k_s = .030''$



$k_s = .060''$

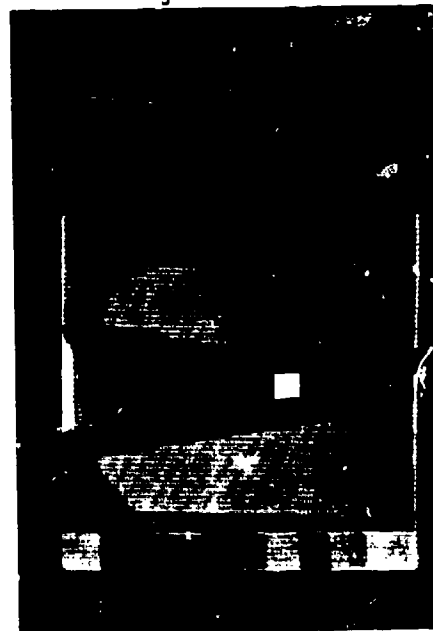


FIGURE 17. REPRODUCTION OF THE COLOR IR PHOTOGRAPHS DEPICTING THE EFFECT OF A ROUGHNESS PATCH ON TRANSITION

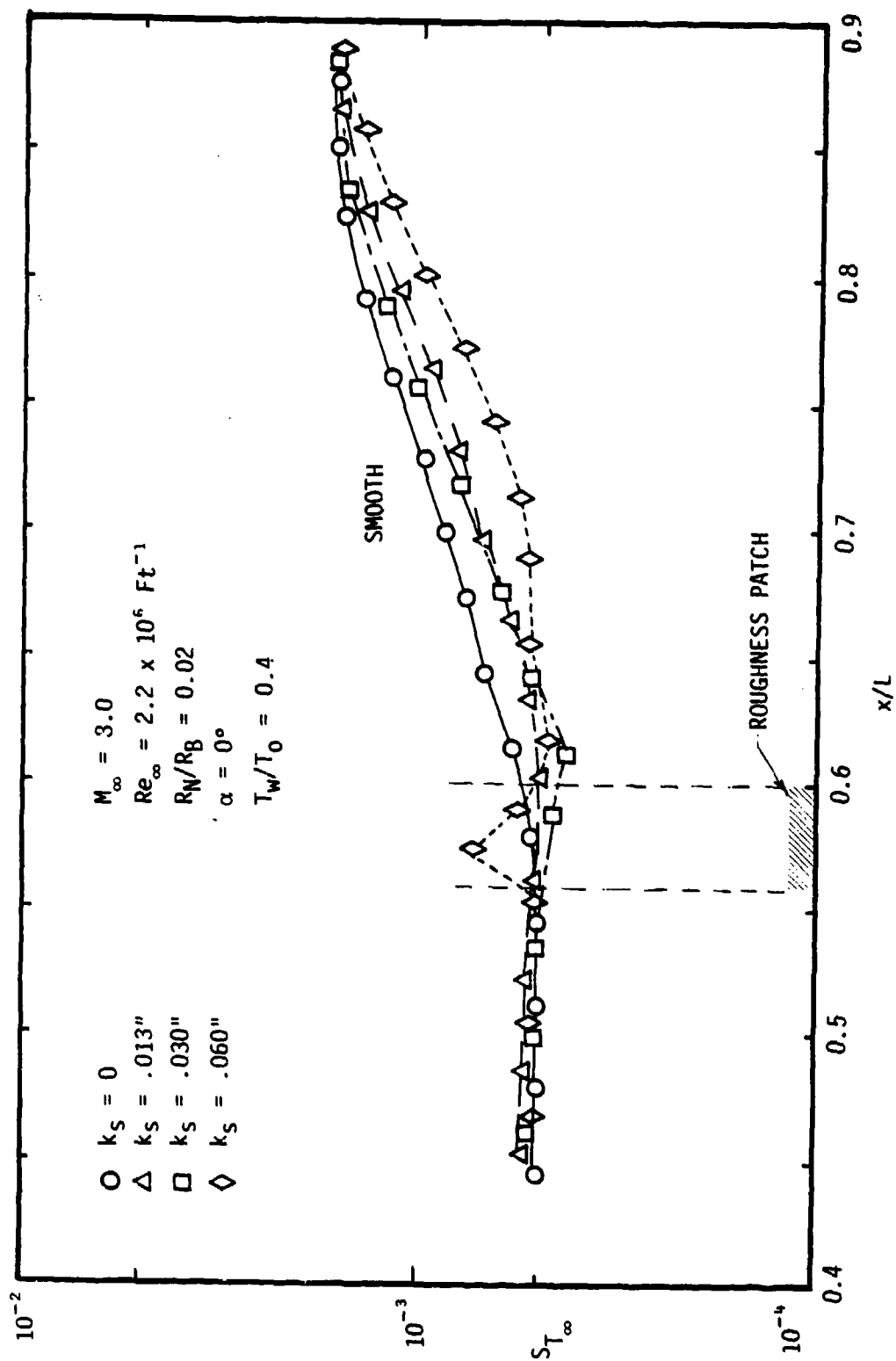


FIGURE 18. EFFECT OF A ROUGHNESS PATCH ON THE SURFACE HEATING DISTRIBUTION/TRANSITION ZONE

transition moves aft. These data are summarized in Figure 19 in terms of a freestream transition Reynolds number versus roughness height, for several values of the bluntness and angle of attack.

The roughness heights selected for this study were scaled, in terms of viscous layer thicknesses, to encompass the magnitudes evident on flight vehicles during reentry. That is, for typical BRVs which undergo transition onset at altitudes of 70-85 KFT, representative values of momentum thickness are from 15 to 20 mils, and displacement thicknesses are from 25 to 50 mils. For the current ground test, the maximum roughness height ($k_s = 60$ mils) was nominally equal to the displacement thickness for $Re_\infty = 2.2$ and $3.8 \times 10^6 \text{ Ft.}^{-1}$. Thus the roughness magnitudes selected for this experiment are within the realm of allowable disturbance levels possible during reentry and therefore the results are applicable for direct comparison.

One possible explanation for the transition delay due to roughness is that the roughness zone promotes increased heating to the surface thereby extracting energy from the stream, which is a stabilizing influence. However, the roughness also enhances turbulence in the stream, which is destabilizing. Obviously, for small roughness, the stabilizing influence dominates, but as it increases the expected destabilizing influence takes over.

It should be stressed that in no case in the current test series was a "turbulent wedge" observed, that is, a region of transitional-turbulent flow which emanated from the roughness site. There always was a delay length from the disturbance site to transition onset. It is evident that the scale of roughness could have been increased to promote transition at that site; however, these roughnesses would not be representative of flight conditions. It should be noted however that the vortex formation at the edge of the roughness patch does promote a localized forward movement of transition relative to the centerline of the roughness site. The increased 3-D effects of this vorticity apparently promotes early transition.

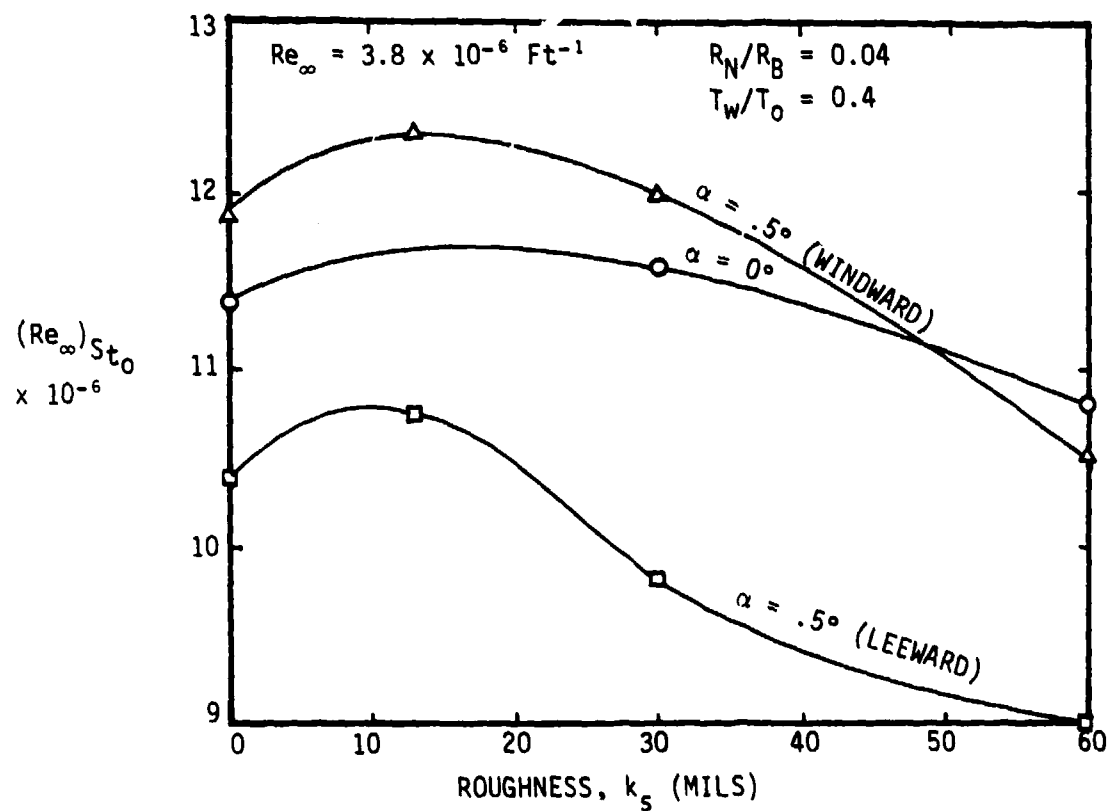
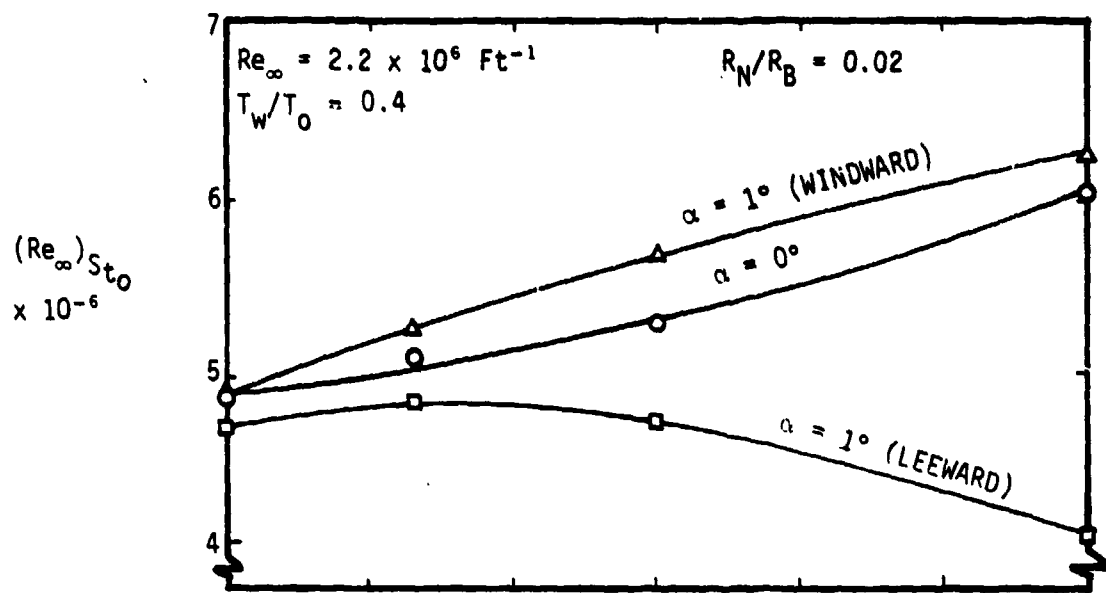


FIGURE 19. FRUSTA ROUGHNESS PATCH EFFECTS ON TRANSITION ONSET

5.4 Frusta Offset Effects

Preprototype and production line flight test vehicles are normally manufactured with several field joints on the frusta for assembly on site. The tolerances are such that there could be a surface discontinuity on assembly at these junctures. System specifications normally require that there be no forward facing step at a joint, and a current operational system requires that the aft facing step, Δ , be no larger than 30 mils. At the transition onset altitude this translates to $\Delta/\delta^* \approx 1.0$ and $\Delta/\theta \approx 3.0$. For the purposes of this ground test, frusta offset values were selected to provide an aft facing step which was equal to or greater than that which exists in flight. Specifically, values of Δ of 75 and 150 mils were selected. In the ground test, at $Re_\infty = 3.8 \times 10^6 \text{ Ft.}^{-1}$ and $R_N/R_B = 0.04$, this translates to the following:

$$\text{for } \Delta = 75 \text{ mils; } \Delta/\delta = 1.0, \Delta/\delta^* = 1.4, \Delta/\theta = 15$$

Shown in Figure 20 are photographs of the IR data for the aft facing frusta offset at $\alpha = 0^\circ$ and 1° , while the complementary heat transfer data are shown in Figure 21. The transition onset data displayed as a function of offset are shown in Figure 22. It is evident from these data that for offset values commensurate with flight test values no effect on transition is observed. As the offset magnitude is increased to 150 mils, a slight effect on transition is observed.

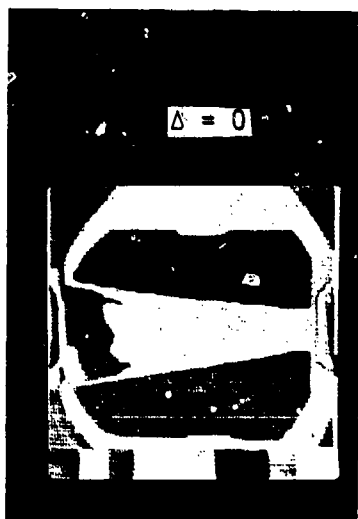
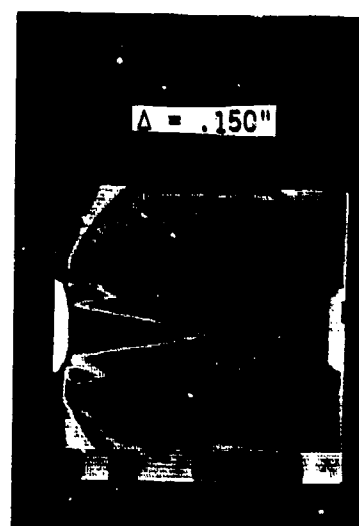
5.5 Frustum Bicone Configuration Effects

Interest in biconic vehicle geometry is a consequence of the potential aerodynamic and vehicle design improvements which may be realized by a modest departure from conical geometry. Figure 23 illustrates the conversion of a cone into a biconic. For a given cone angle and base diameter, warhead forward diameter establishes the most aft biconic break station which can be accommodated without shifting the warhead aft. For vehicles of current interest, break station radii are 0.4 to 0.5 of R_B .

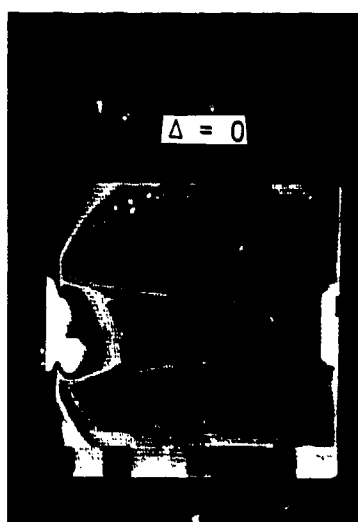
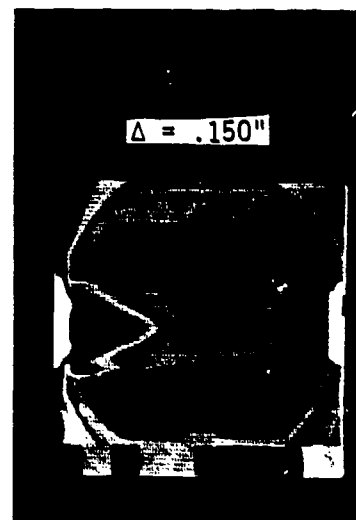


$M_{\infty} = 8.0$
 $Re_{\infty} = 3.8 \times 10^6 \text{ Ft}^{-1}$
 $R_N/R_B = 0.04$

$\alpha = 1^\circ$
 LEeward



$\alpha = 0^\circ$



$\alpha = 1^\circ$
 WINDward

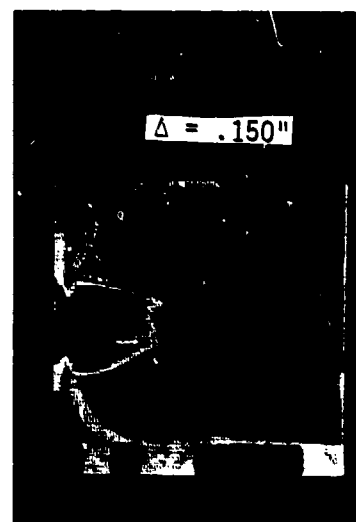


FIGURE 20. REPRODUCTION OF THE COLOR IR PHOTOGRAPHS DEPICTING
 THE EFFECT OF FRUSTA OFFSET (AFT FACING) ON TRANSITION

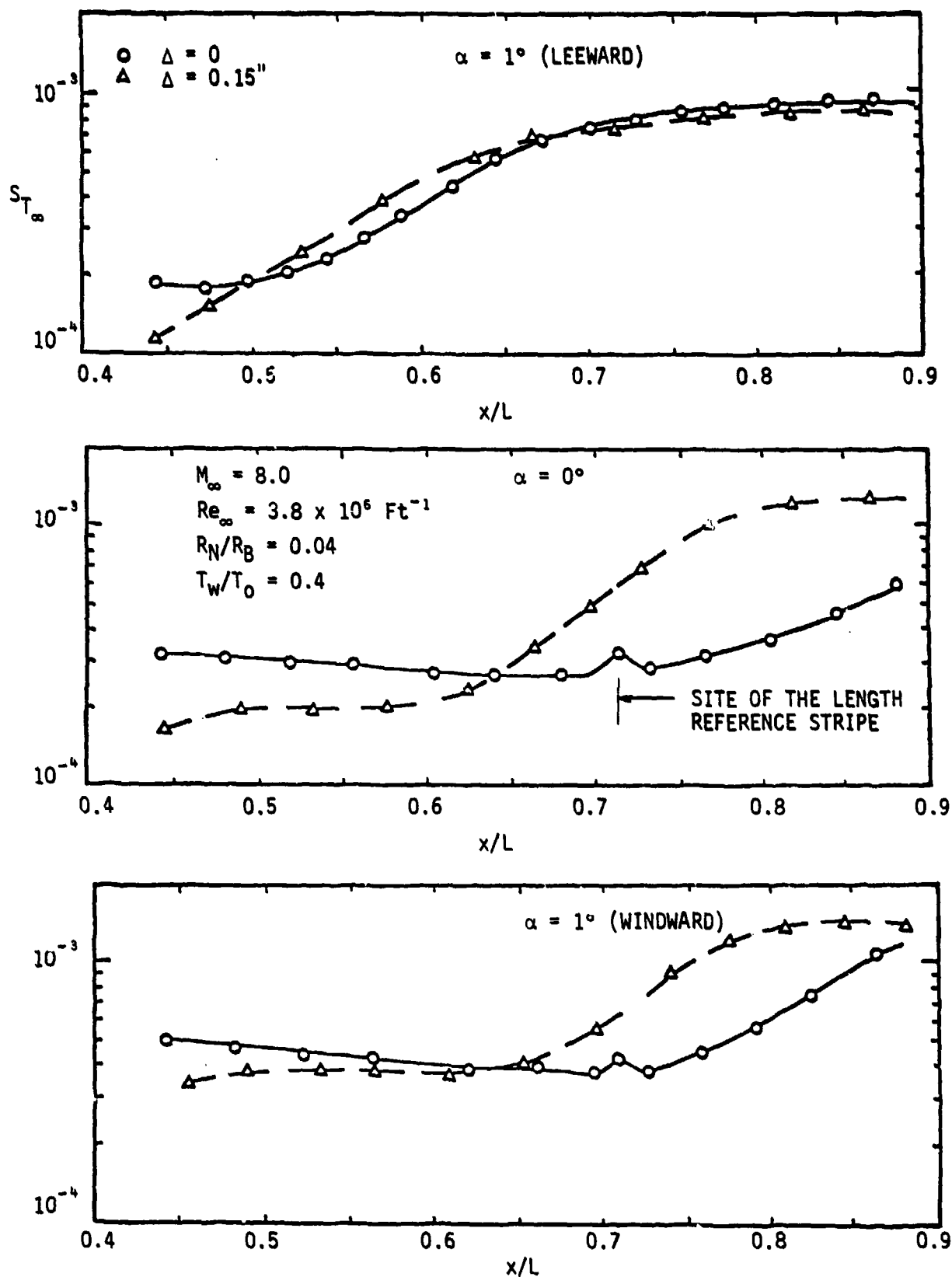


FIGURE 21. EFFECT OF AFT FACING FRUSTA OFFSET ON THE SURFACE HEATING DISTRIBUTION/TRANSITION ZONE

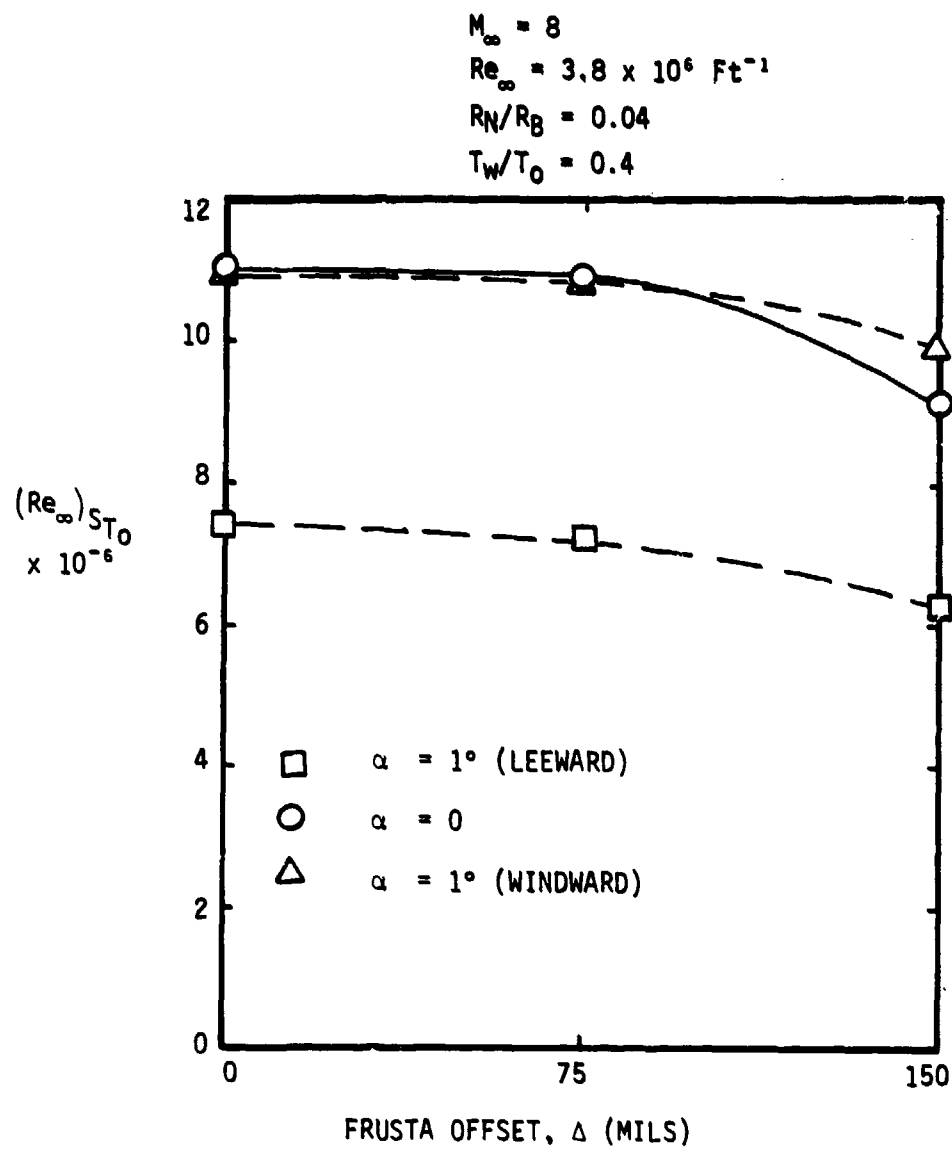


FIGURE 22. FRUSTA OFFSET EFFECTS ON TRANSITION ONSET (AFT FACING)

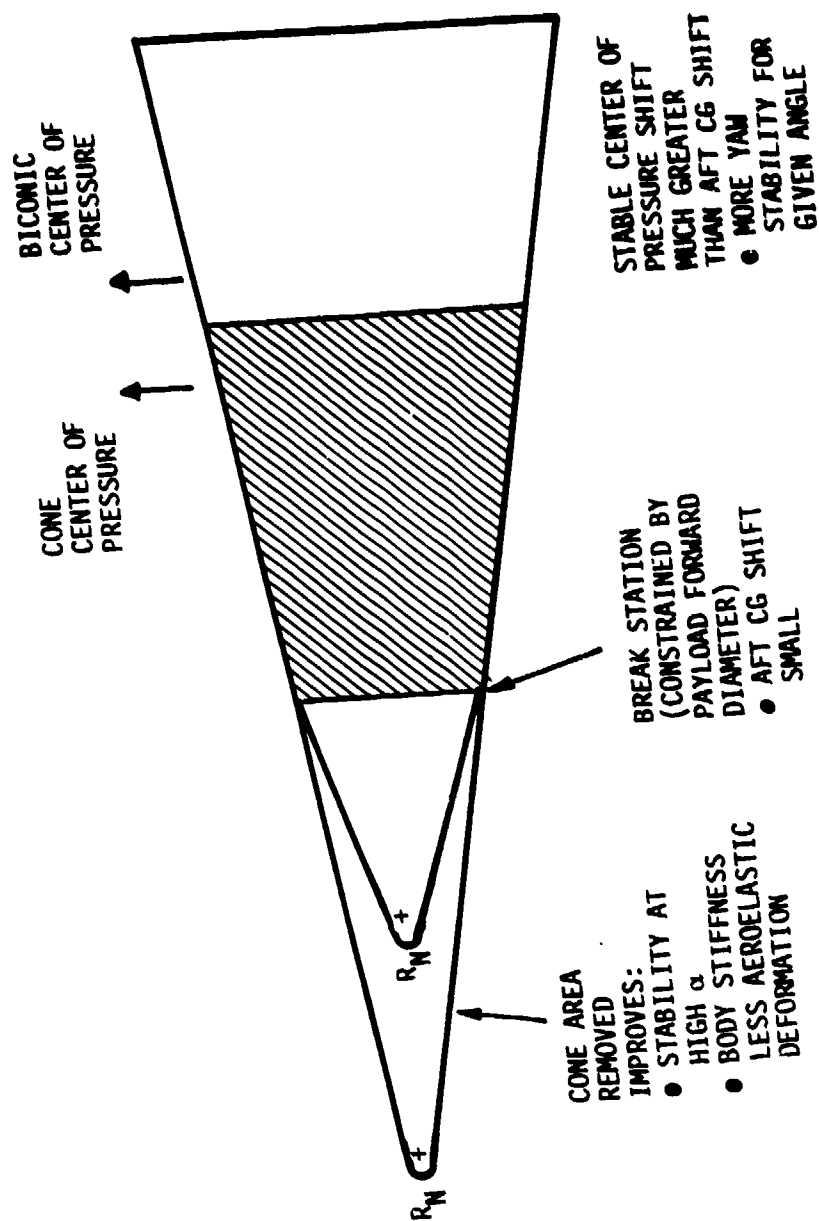


FIGURE 23. COMPARISON OF AERO CHARACTERISTICS—CONES AND BICONICS

The planform area thus removed from the forward portion of the cone results in a more aft center of pressure at angle of attack (Figure 24). Center of gravity is shifted aft a relatively small amount by this modification. Consequently a net increase in stability results which may be used to reduce ballast or shorten the vehicle. The latter results in a decrease in vehicle diameter for a given cone angle. Thus it is seen that the biconic geometry offers a more packageable, shorter length, lighter vehicle.

The objective of this subset of tests is to establish the transition performance of bicone vehicles relative to their straight cone counterparts. As indicated earlier, tests were conducted for $13^\circ/7^\circ$, $10^\circ/7^\circ$, and $7^\circ/7^\circ$ bicones, with the break radius at 40% of R_B , as shown in Figure 1. Data were obtained over an angle of attack range of $\pm 1^\circ$, consistent with RVs' low altitude α excursions. At zero angle of attack the data indicate that, for fixed freestream conditions, transition moves aft slightly with increasing forecone angle (i.e., occurs closer to the vehicle base) as shown in Figure 25a. The aft movement is more pronounced for the sharp configurations. For blunted configurations, the variation is relatively small such that for flight conditions one would not expect to detect an effect on the transition onset altitude (i.e., within ± 5 KFT). This conclusion is in partial agreement with the results of Stetson¹³ who also did not see significant effects of bicone geometry on transition onset for blunt bodies.

It is interesting to note however that the degree of asymmetry - wind to lee - noted for the bicones is significantly smaller than that for the straight cones (Figures 25b and 25c), both sharp and blunt.

The general conclusions that could be drawn from these limited bicone data indicate that the transition performance of biconic BRVs would be comparable to straight cone BRVs (i.e., for a given base diameter vehicle). That is, the transition altitude would not be materially affected, and the vehicle would be slightly less prone to transition dispersion.

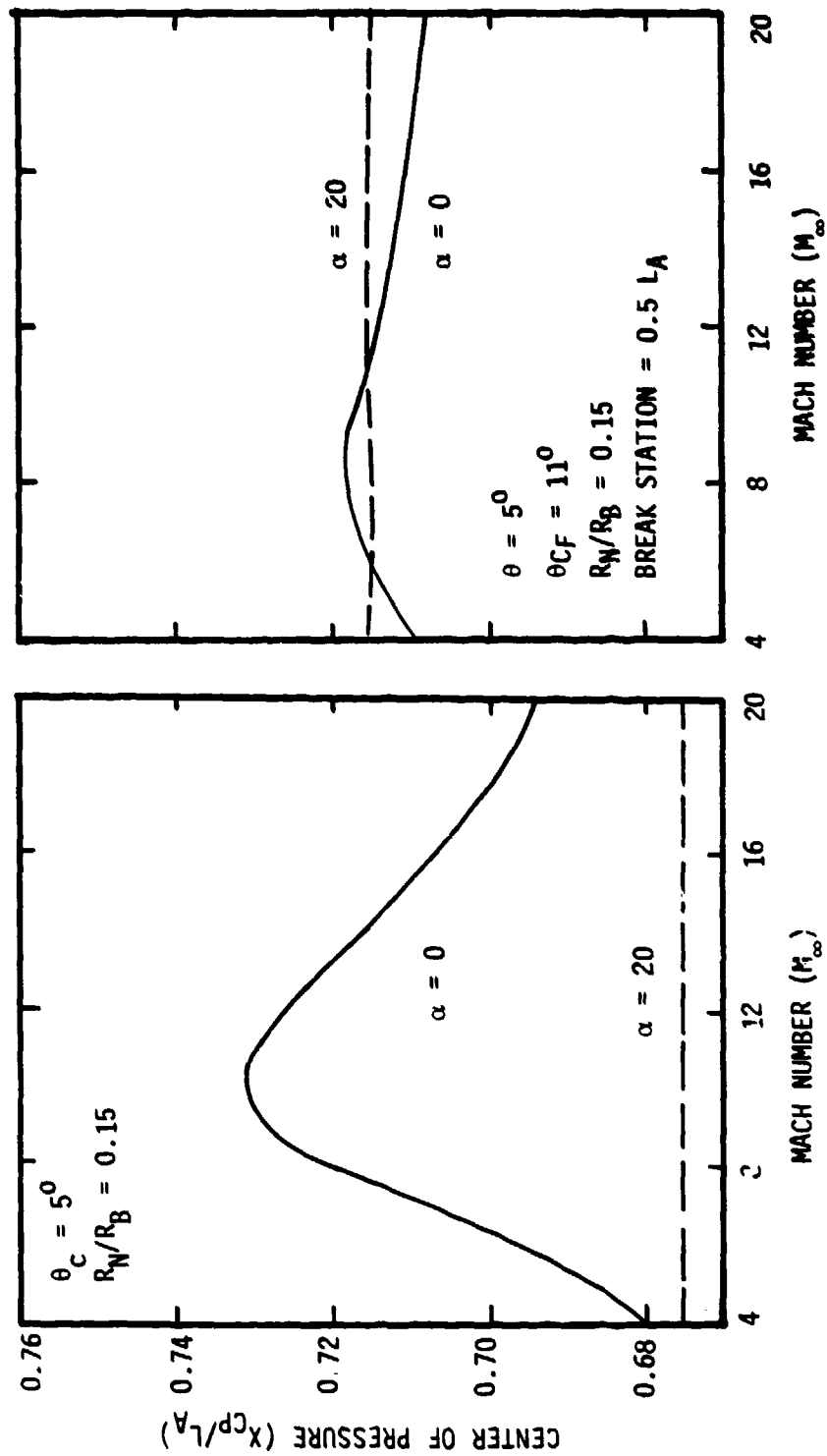
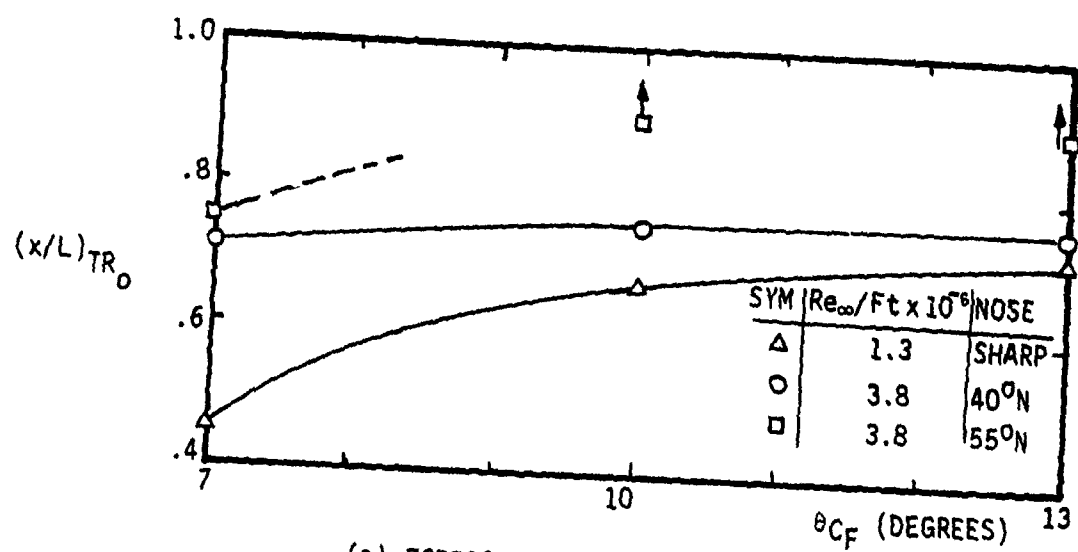
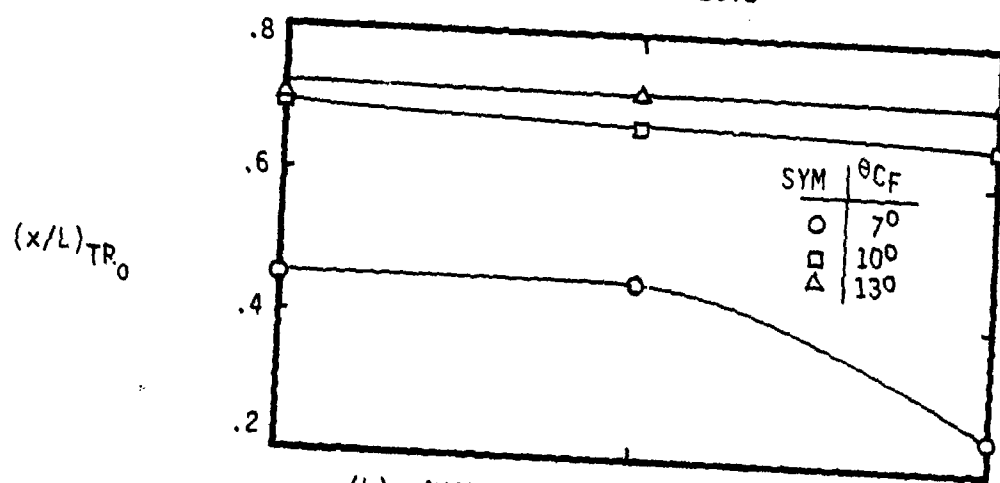


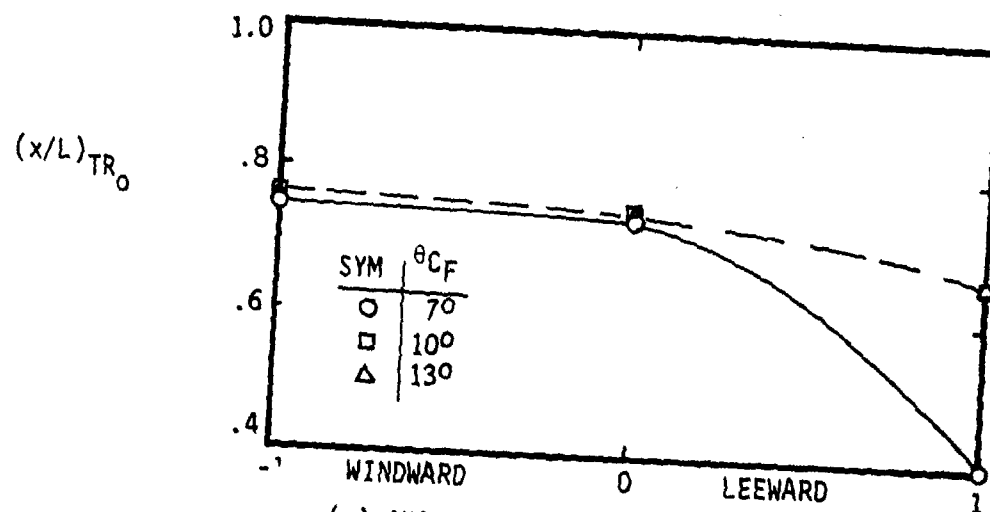
FIGURE 24. CENTER OF PRESSURE VARIATION WITH MACH NUMBER



(a) FORECONE ANGLE EFFECTS



(b) ANGLE-OF-ATTACK EFFECTS - SHARP NOSE
($Re_\infty/Ft. = 1.3 \times 10^6$)



(c) ANGLE-OF-ATTACK EFFECTS - 40°N NOSE
($Re_\infty/Ft. = 3.8 \times 10^6$)

FIGURE 25. EFFECT OF BICONE GEOMETRY ON TRANSITION ONSET ($M_\infty = 8$)

6.0 SUMMARY AND CONCLUSIONS

An experimental program was conducted to investigate the transition performance of vehicles with: (a) non-sphere cone geometries, and (b) local aberrations such as misaligned frusta sections and localized roughness patches which could be attributed to antenna windows.

The tests were performed at the AEDC von Karman facility in Tunnel B at Mach 8. Boundary layer transition was deduced from the surface heating profiles inferred from the AEDC infrared scanning system data. The model used for this investigation was fabricated from an epoxy material whose insulating and emissive properties make it well suited for IR system usage. Tests were conducted over a range of Reynolds numbers from 1.3×10^6 to 3.8×10^6 per foot, and an angle of attack range from 0° to 2° .

It was concluded that the AEDC infrared system provides an extremely useful technique for deducing the heat transfer distribution on the surface of a model. The heat transfer inferred from the IR data are in excellent agreement with theory and with data obtained from other sources such as the thin skin 1-D approach. Furthermore, the current status of this equipment at AEDC enables the test engineer to utilize the data output on a real time basis to guide subsequent test directions.

Relative to the primary objectives of this investigation, the following are the major summary conclusions obtained:

1. In the small spherical bluntness range (i.e., $R_N/R < .08$), as R_N is increased transition is delayed and also provides less asymmetry at angle of attack

2. Preshaped noses affect transition such that, for a prescribed r/R_B ; bluff shapes delay transition onset and provide less asymmetry at angle of attack, and sharper shapes promote earlier transition onset and have greater asymmetries due to angle of attack. These results, coupled to analytic predictions of RV stability with bluff non-spherical nose shapes, indicate that improved BRV low altitude performance (i.e., <100 KFT) could be achieved - provided the nosetip remained bluff.
3. Roughness patches on the frusta of a magnitude commensurate with flight (i.e., $k_s/\delta^* \leq 1$) do not promote early transition; therefore, turbulent wedges probably do not exist. In particular, for small roughness, $k_s/\delta^* < 1$, transition onset delays may be observed.
4. Frusta offset with aft facing steps of magnitudes commensurate with flight vehicles (i.e., $\Delta/\delta^* \leq 1.0$) probably do not promote early transition.
5. The biconic configurations investigated produced (a) a delay in transition onset relative to the straight cone for the sharp configuration, and (b) a slight-to-imperceptible delay for the blunt cases. However, the degree of asymmetry with angle of attack - wind to lee - was significantly reduced for all bicones tested compared to straight cone results. These data, coupled with predictions of RV stability, indicate that one would expect smaller stability excursions with Mach number for bicones compared to straight cones, thereby resulting in reduced dispersion during reentry.

In addition to these summary conclusions, the following observations were also made:

1. The data obtained in the current investigation agree well with the results of other experimenters taken in several test facilities and with several different types of instrumentation. These data show that spherical bluntness and angle of attack trends are not facility dependent.
2. The rearward displacement of transition due to spherical nose bluntness was found to be sensitive to freestream Mach number for values of $Re_{\infty N} \leq 10^5$.
3. For small bluntness, transition was found to move aft on the cone until a maximum rearward displacement was observed at $Re_{\infty N} \leq 10^5$.
4. As shown in the literature, a bluntness reversal was observed such that increasing nose bluntness caused transition to move forward on the cone with increasing $Re_{\infty N}$ (i.e., $>10^5$).
5. For large bluntness, $Re_{\infty N} > 10^5$, the transition dependence on Mach No. is significantly smaller than for the small bluntness case (see Figure 10). Although the available data are sparse, transition dependence on Mach Number at large $Re_{\infty N}$ is reversed relative to the small bluntness data. That is, for small $Re_{\infty N}$, transition Reynolds number increases with increasing Mach number; for large $Re_{\infty N}$ transition Reynolds number decreases with increasing Mach number. More data are required to quantify this observation.

REFERENCES

1. Bynum, D. S., Hube, F. K., Key, C. M., and Dyer, P. M., "Measurement and Mapping of Aerodynamic Heating in VKF Tunnel B with an Infrared Camera," AEDC-TR-76-54, November 1976.
2. Hube, F. K., "Simulated Thermal Protection Tile Roughness Effects on Windward Surface Heat Transfer on the Rockwell International Space Shuttle Orbiter, AEDC-TR-76-98, January 1977.
3. Boylan, D. E., Carver, D. B., Stallings, D. W., and Trimmer, L. L., "Measurement and Mapping of Aerodynamic Heating Using a Remote Infrared Scanning Camera in Continuous Flow Wind Tunnels," AIAA Paper 78-799, April 1978.
4. Stallings, D. W., "Infrared Mapping of Boundary Layer Transition on a Slender Cone," AEDC-TSR-79-V14, March 1979.
5. Martellucci, A. and Neff, R. S., "Influence of Asymmetric Transition on Reentry Vehicle Characteristics," J. Spacecraft and Rockets, 8, Number 5, p. 476-482, May 1971.
6. Stetson, K. F. and Rushton, G. H., "Shock Tunnel Investigation of Boundary Layer Transition at $M = 5.5$," AIAA Journal, Vol. 5, pp. 899-906, May 1967.
7. Softley, E. J., "Boundary Layer Transition on Hypersonic Blunt, Slender Cones," AIAA Paper No. 69-705, June 1969.
8. Blottner, F. G., "Finite-Difference Methods of Solution of the Boundary Layer Equations," AIAA Journal, 8, 2, pp. 193-205, February 1970.
9. Hall, D. W., "The Three-Dimensional Shock and Pressure (3DSAP) Approximate Flow Field Technique," SAMSO TR-77-C-145, May 1977.
10. Holden, M. S., "Studies of the Effects of Transitional and Turbulent Boundary Layers on the Aerodynamic Performance of Hypersonic Re-entry Vehicles in High Reynolds Number Flows," AFOSR-TR-79-0125, December 1978.
11. Muir, J. F. and Trujillo, A. A., "Effects of Nose Bluntness and Free Stream Unit Reynolds Number on Slender Cone Transition at Hypersonic Speeds," Proceeding of the Boundary Layer Transition Workshop, Vol. III, 20 Dec. 1971, Aerospace Report No. TOR-0172 (S2816-16)-5.
12. Martellucci, A. and Laganelli, A., "Downstream Effects of Gaseous Injection Through a Porous Nose," GE TIS 71SD218, February 1971 (also AIAA Paper 72-185).
13. Stetson, K. F., "Effects of Nose Bluntness and Angle of Attack on Boundary Layer Transition on Cones and Biconic Configurations," AIAA Paper 79-0269, January 1979.

APPENDIX A

INFRARED (IR) SYSTEM DESCRIPTION

The infrared system at AEDC, which employs an AGA Thermovision 680 camera, is a completely passive system that can be used to map the heating on a body, its output can be amplified, converted from analog-to-digital form, and reduced to heat transfer coefficients. Infrared radiation emitted from the model surface passes through the tunnel atmosphere, window, lens, and scanning optics and is focused on the detector in the IR camera. The IR energy is then converted by the detector into an analog voltage that is displayed on a color video monitor and digitized by an analog-to-digital (A-D) converter. Output of the A-D converter is interfaced to the computer for reduction to aerodynamic heating rates.

Infrared energy is emitted in the electromagnetic spectrum from about 0.7 to 1,000 μm . The AGA 680 camera employs a detector sensitive to the range between 3 and 5.8 μm . The infrared radiation collected by the system optics is focused on the detector, which produces an electrical signal proportional to the total energy in that bandwidth.

Planck's law gives the relationship between the spectral radiant emittance of a blackbody radiator and its temperature as

$$W_{\lambda b} = \frac{2 Hc^2}{\lambda^5 (e^{Hc/\lambda KT} - 1)} \quad A-(1)$$

Integration of Planck's relationship over wavelengths from zero to infinity yields the Stefan-Boltzmann law which relates total radiant energy and temperatures for a blackbody as

$$W = \sigma T^4 \quad A-(2)$$

Real objects do not behave as true blackbodies because of absorbed, reflected, and transmitted radiation. The Stefan-Boltzmann law can be modified for a graybody by simply multiplying the right-hand side of Eq. A-(2) by the surface emissivity, yielding

$$W = \epsilon \sigma T^4 \quad A-(3)$$

where an emissivity of unity corresponds to a blackbody.

All physical objects have an emissivity less than unity which is usually dependent on wavelength. In applications such as the one discussed here, where accurate object temperature measurements are required, the variation of the surface emissivity as a function of wavelength and camera view angle is important and must be determined experimentally.

Details of the IR camera used in the AEDC-VKF are illustrated in Figures A-1 and A-2. This is a scanning optical-mechanical camera which does not use film. The camera scans the model to produce a complete picture at the rate of 16 frames per second. The schematic in Figure A-2 shows the liquid-nitrogen-cooled (indium-antimonide) detector and the rotating prisms which control the position of the instantaneous field-of-view. An IRTAN 2 window is used in the viewing path because the conventional materials used in wind tunnel windows are opaque to radiation in the bandwidth range of interest.

The scanning apparatus consists of two rotating (vertical and horizontal) prisms, two prism-drive motors, magnetic position-sensing heads, and a collimating lens. A virtual image is formed by the front lens of the camera on a plane within the first prism. The image is scanned vertically by rotation of the prism about its horizontal axis. This results in a horizontal, virtual line-image being formed within the second scanning prism. The line-image is then scanned horizontally in turn by rotation of the second prism about its vertical axis.

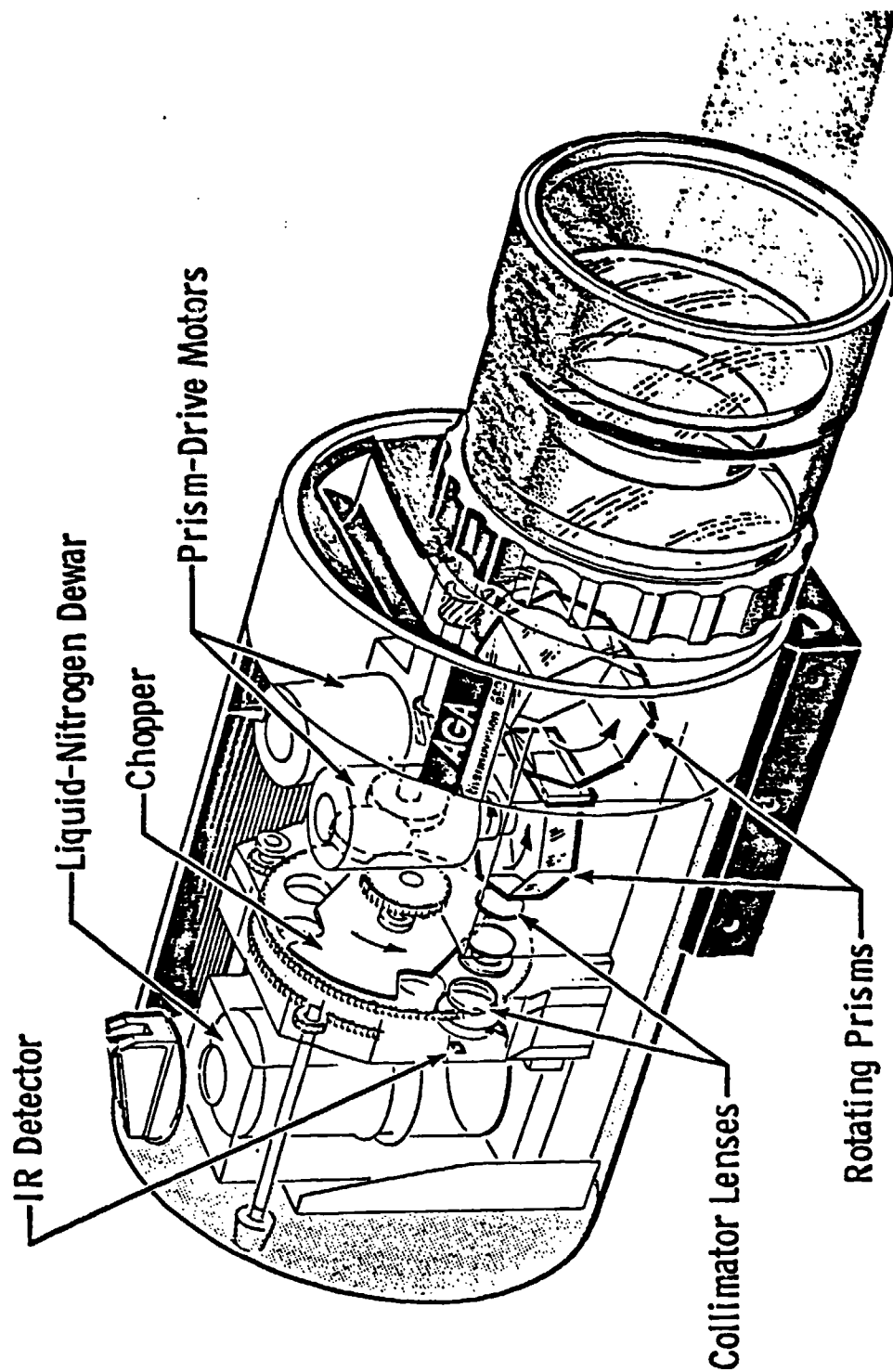


FIGURE A-1. INFRARED SCANNING CAMERA OVERALL GEOMETRY

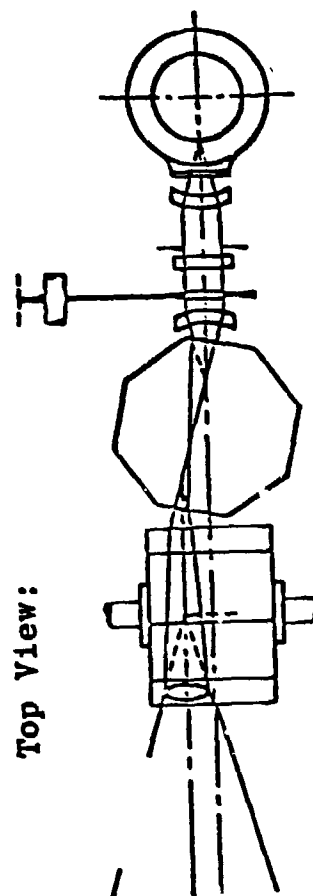
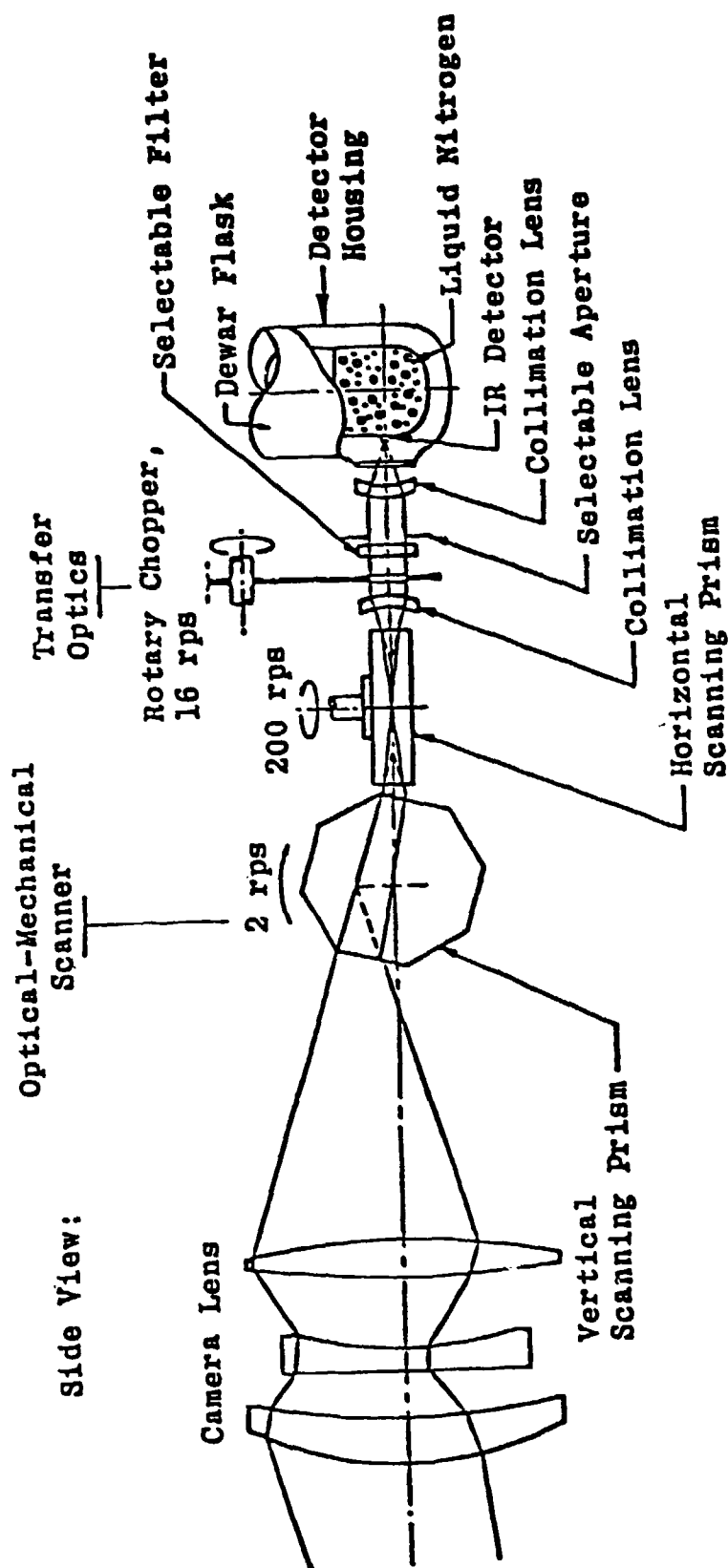


FIGURE A-2. INFRARED SCANNING CAMERA INTERNAL LAYOUT

One complete frame of IR data consists of 70 scan lines with 110 points per line for a total of 7700 discrete but overlapping spots. For most test installations the field-of-view is such that the model does not fill the complete frame. In order to save computer storage space, only that portion of the frame which contains model data is digitized. For the current test, the area of interest was 27 lines by 83 points which corresponds to 2241 spots. For each point, the camera output is digitized and converted to a temperature by means of Equations A-(1) - A-(3) which incorporate constants peculiar to this system. These constants are derived from laboratory calibrations using a standard blackbody source.

Reduction of the infrared data is based on the assumption that the surface temperature history is that of a homogeneous, semi-infinite slab subjected to a constant heat-transfer coefficient. The surface temperature rise is then given by:

$$\frac{T_w - T_i}{T_o - T_i} = 1 - e^{\beta^2} (\text{erfc } \beta) \quad \text{A- (4)}$$

where

$$\beta = h \frac{\sqrt{\Delta t}}{\sqrt{\rho C_p k}} \quad \text{A- (5)}$$

The temperature calculated for each spot is used in Equation A-4 to evaluate β . The heat transfer coefficient, h , is then calculated from Equation using a time interval (Δt) based on the time at which the IR frame was digitized. The heat transfer coefficient calculated from Equation presented in terms of the nondimensional Stanton number using

$$S_{T_\infty} = \frac{h}{\rho_\infty V_\infty} \left(\frac{T_o - T_w}{H_o - H_w} \right) \quad \text{A- (6)}$$

This value was normalized using the Fay Riddell stagnation point heat transfer coefficient (Reference A-1*) defined as:

$$(S_T)_{FR} = \frac{8.17 P_{t2}^{0.5} \mu_0^{0.4} \left[1 - \frac{P_\infty}{P_{t2}}\right]^{0.25}}{\rho_\infty V_\infty R_N^{0.5} T_0^{0.15}} \quad A-(7)$$

where

P_{t2} - Stagnation pressure downstream of a normal shock wave, psia

μ_0 - Air viscosity based on T_0 , lbf-sec/ft²

P_∞ - Free-stream pressure, psia

T_0 - Tunnel stilling chamber temperature, °R

R_N - Reference nose radius, ft
(1.0 ft for this test)

ρ_∞ - Free-stream density, lbm/ft³

V_∞ - Free-stream velocity, ft/sec

The tabulated IR data consists of the calculated surface temperature (ratioed to the model initial temperature, T_i) and the normalized Stanton number for each of the 2241 spots in the data area of the IR frame.

The output of the IR camera is displayed in real time on a color television monitor. A 70-mm camera was used to photograph the monitor screen simultaneously with the single frame digitizing process. A sample photograph is presented in Figure A-3. On the television monitor the total temperature range which the system is set up to measure is divided, in a nonlinear fashion, into ten separate colors, starting with blue for the lowest temperature and progressing through white for the highest. Each color then represents a temperature band within the total range, and the interface between two colors corresponds to one particular temperature. For this test the color band was not calibrated, so the photographs were not useful for quantitative data. However, they do provide a view of the overall heat-transfer pattern which cannot be seen in the tabulated data.

*A-1 - Fay, J. A. and Riddell, F. R., "Theory of Stagnation Point Heat Transfer in Dissociated Air," Journal of the Aeronautical Sciences, Vol. 25, No. 2, February 1958.

GROUP NUMBER

← FLOW

U.S. AIR FORCE PHOTO-ABC
AIR, INC., ABC DIVISION
A SECURITY CONSULTING COMPANY
4000 S. 10TH AVE., SUITE 100
DENVER, CO 80202
TEL: 303-733-1111
FAX: 303-733-1112
WWW.AIR-ABC.COM

FIGURE A-3. SAMPLE INFRARED PHOTOGRAPH

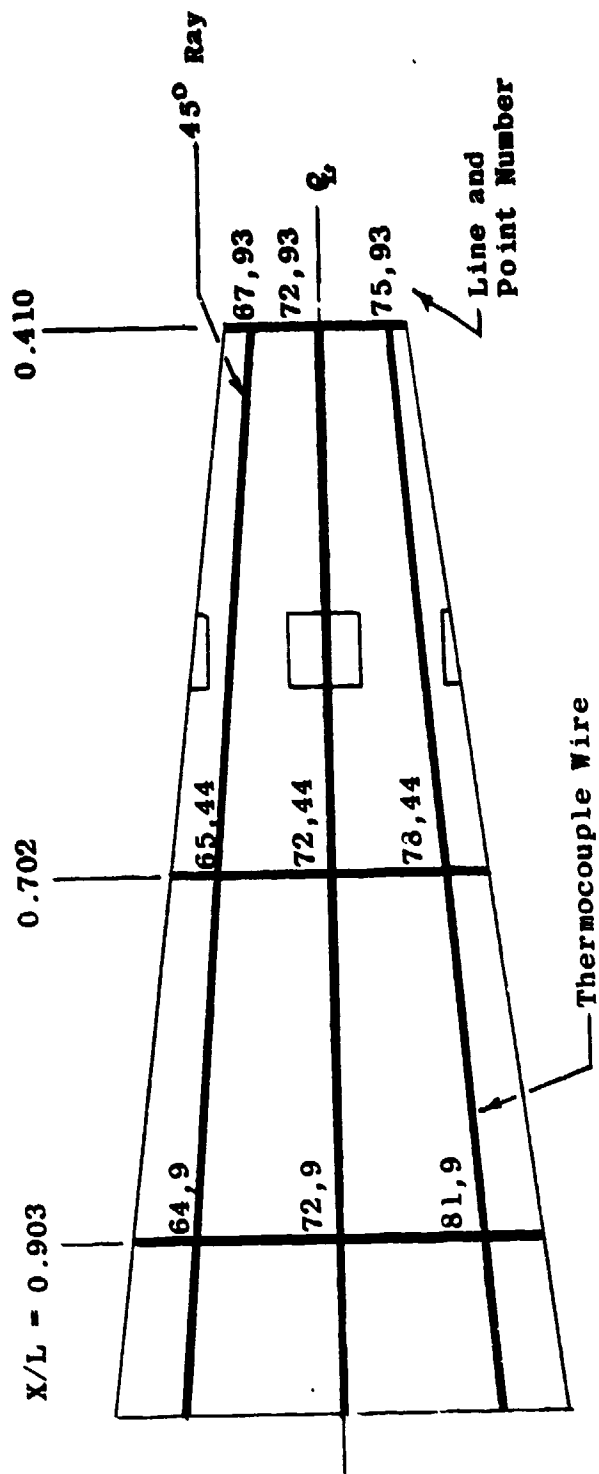


FIGURE A-4, GRID-LINE PATTERN

In order for the IR data to be useful in making plots of heat-transfer coefficients versus model coordinates, it is necessary to define model position in terms of Line and Point numbers. This was done by taking pretest infrared scans of the model with a grid-line pattern attached. Thermocouple wire was used to form the pattern, and, when connected to a power supply, the wire became hotter than the surrounding model surface and thus could be seen quite clearly in the infrared picture.

The dimensions of the grid pattern are shown in Figure A-4. The wires at $X/L = 0.410$ and 0.903 define the axial extent of the IR field-of-view. The wires in the axial direction were placed along the model centerline and along rays which were at 45-deg angles around the body from the centerline. Pretest experiments had established that this was a practical limit for the area of valid data. Beyond this limit the effective emissivity decreases rapidly due to the model curvature.

The pairs of numbers indicated at several of the thermocouple wire intersections are the IR Line and Point numbers, respectively, which define the locations of the intersections within the IR picture. With this information and the accompanying model dimensions, any spot on the model can be related to a spot in the IR picture. Using the data of Figure A-4, the relationship between IR Point number and the nondimensional distance along the model axis, X/L , was determined to be

$$X/L = 0.96 - (5.857 \times 10^{-3}) (\text{Point number}) \quad A-(8)$$

It should be noted that for this test the accuracy with which a given point on the model can be located within the IR frame was approximately ± 0.25 in., as determined from grid pattern scans conducted several times during the test.

Test Procedure

In the VKF continuous flow wind Tunnel B, the model is mounted on a sting support mechanism in an installation tank directly underneath the tunnel test section. The tank is separated from the tunnel by a pair of fairing doors and a safety door. When closed, the fairing doors, except for a slot for the pitch sector, cover the opening to the tank and the safety door seals the tunnel from the tank area. After the model is prepared for a data run, the personnel access door to the installation tank is closed, the tank is vented to the tunnel flow, the safety and fairing doors are opened, the model is injected into the airstream, and the fairing doors are closed. After the data are obtained, the model is retracted into the tank. The model is then cooled by a series of air jets directed at the viewing surface. This continues until the surface temperature is nominally at the pretest value. The sequence is reversed with the tank being vented to atmosphere to allow access to the model in preparation for the next run. The sequence is repeated for each configuration change.

Instrumentation outputs were recorded using the VKF digital data scanner in conjunction with the VKF analog subsystem. Data acquisition from all instruments other than the infrared camera was under the control of a PDP 11/40 computer, utilizing the random access data system (RADS).

A given injection cycle where the model is exposed to the flow for 10 to 30 seconds is termed a group, and all the data obtained is identified in the data tabulations by a group number.

TEST CONDITIONS AND DATA UNCERTAINTY

Uncertainties in the tunnel free-stream parameters and the model aerodynamic coefficients were estimated using the Taylor series method of error propagation; namely,

$$(\Delta F)^2 = \left(\frac{\partial F}{\partial X_1} \Delta X_1 \right)^2 + \left(\frac{\partial F}{\partial X_2} \Delta X_2 \right)^2 + \left(\frac{\partial F}{\partial X_3} \Delta X_3 \right)^2 \dots + \left(\frac{\partial F}{\partial X_n} \Delta X_n \right)^2 \quad A-(9)$$

where ΔF is the absolute uncertainty in the dependent parameter $F = f(X_1, X_2, X_3 \dots X_n)$ and X_i are the independent parameters (or basic measurements). ΔX_i are the uncertainties (errors) in the independent measurements (or variables).

A summary of the nominal test conditions for which data were obtained is given below.

<u>MACH</u>	<u>P₀, psia</u>	<u>T₀, °R</u>	<u>q_∞ , psia</u>	<u>p_∞ , psia</u>	<u>Re x 10⁻⁶/ft</u>
7.88	82	1275	0.4	0.01	0.4
7.96	275	1290	1.3	0.03	1.3
7.98	450	1295	2.1	0.05	2.2
8.00	870	1340	4.1	0.09	3.8

The accuracy (based on 2σ deviation) of the basic tunnel parameters, determined from test section flow calibrations, were used to estimate uncertainties in the other free-stream properties using Equation A-(9). The computed uncertainties in the tunnel free-stream conditions for Mach 8 are summarized below:

Uncertainty, (+) percent of actual value

<u>MACH</u>	<u>P_∞</u>	<u>q_∞</u>	<u>RE/ft</u>
0.4	2.5	1.7	1.2

The uncertainty in model angle-of-attack is estimated to be ±0.05 deg. For boundary layer transition purposes, the model angle-of-attack was a critical parameter; as a result, it was set in the tank below the tunnel

prior to injection into the flow and verified using an inclinometer, rather than relying entirely on the sector position indicator. The model was then locked into position for the run.

Heat-transfer coefficient measurements for the IR runs ranged from about 2×10^{-4} to 2×10^{-3} Btu/ft²-sec-°R. Overall estimated uncertainty in absolute values of heat-transfer coefficient for this technique are:

<u>h , Btu/ft²-sec-°R</u>	<u>Uncertainty \pm, percent</u>
2×10^{-4}	21
2×10^{-3}	15

The above uncertainty values were derived using the previously discussed Taylor series method of error propagation with the instrumentation accuracies combined with the accuracies below:

<u>Item</u>	<u>Estimated Precision (\pm)</u>
$\sqrt{\rho c_p k}$	10% of measured value
T_i	1% of measured value
$(T_w)_{IR}$	1% of measured value
T_o	0.4% of measured value
Δt	0.1 sec absolute

The uncertainties in heat-transfer coefficient are applicable for time intervals greater than five seconds, provided that the semi-infinite-solid assumption is not violated. It should be noted that the dominant term in the uncertainty calculations for IR techniques is the accuracy of the model thermal properties data ($\rho c_p k$).

DISTRIBUTION LIST

Ballistic Missile Office
BMO/SYDT
Attn: Maj. K. Yelmgren (2)
Norton AFB, CA 92409

Defense Technical Information Center (2)
Cameron Station
Alexandria, VA 22314

Air University Library
Maxwell AFB, AL 36112

TRW DSSG
Attn: W. Grabowsky (2)
P. O. Box 1310
San Bernardino, CA 92402

TRW Systems Group (2)
Attn: J. Ohrenberger
M. Gyetvay
1 Space Park
Redondo Beach, CA 92078

Headquarters, Arnold Engineering
Development Center
Arnold Air Force Station
Attn: Library/Documents
Tullahoma, TN 37389

Armament Development and Test Center
Attn: Technical Library, DLOSL
Eglin AFB, FL 32542

Air Force Wright Aeronautical Laboratories (3)
Air Force Systems Command
Attn: M. Buck (AFWAL/FIM)
R. Neumann (AFWAL/FIMG)
V. Dahlem (AFWAL/FIMG)
Wright-Patterson AFB, OH 45433

U. S. Army Ballistic Missile
Defense Agency/ATC-M
Attn: J. Papadopoulos
P. O. Box 1500
Huntsville, AL 35807

Director, Defense Nuclear Agency
Attn: J. Somers (SPAS)
Washington, DC 20305

Naval Surface Weapons Center
Attn: Carson Lyons/K06
White Oak Laboratories
Silver Spring, MD 20910

Acurex Aerotherm
Aerospace Systems Division
Attn: C. Nardo
485 Clyde Avenue
Mountain View, CA 94042

Avco Systems Division
Attn: N. Thyson
201 Lowell Street
Wilmington, Mass 01887

General Electric Company
Attn: R. Neff
3198 Chestnut Street
Philadelphia, PA 19101

Lockheed Missiles and Space Co.
P. O. Box 504
Attn: G. T. Chrusciel
Sunnyvale, CA 94086

McDonnell Douglas Astronautics Co.
Attn: J. Copper
5301 Bolsa Avenue
Huntington Beach, CA 92647

PDA Engineering
Attn: M. Sherman
1560 Brookhollow Drive
Santa Ana, CA 92705

Sandia Laboratories
P. O. Box 5800
Attn: Library
Albuquerque, NM 87115

Science Applications, Inc.
Attn: A. Martellucci
994 Old Eagle School Road
Suite 1018
Wayne, PA 19087